

# Machine-learning for photoplethysmography analysis: Benchmarking feature, image, and signal-based approaches

Mohammad Moulaeifard<sup>1</sup>, Loic Coquelin<sup>2</sup>, Mantas Rinkevičius<sup>3</sup>,  
Andrius Sološenko<sup>3</sup>, Oskar Pfeffer<sup>4</sup>, Ciaran Bench<sup>5</sup>, Nando  
Hegemann<sup>4</sup>, Sara Vardanega<sup>6</sup>, Manasi Nandi<sup>6</sup>, Jordi Alastruey<sup>6</sup>,  
Christian Heiss<sup>7</sup>, Vaidotas Marozas<sup>3</sup>, Andrew Thompson<sup>5</sup>, Philip J.  
Aston<sup>5,8</sup>, Peter H. Charlton<sup>9</sup>, and Nils Strodthoff<sup>1</sup>

<sup>1</sup>Carl von Ossietzky Universität Oldenburg, Oldenburg, Germany

<sup>2</sup>Laboratoire national de métrologie et d'essais, Paris, France

<sup>3</sup>Biomedical Engineering Institute, Kaunas University of  
Technology, Kaunas, Lithuania

<sup>4</sup>Physikalisch-Technische Bundesanstalt, Berlin, Germany

<sup>5</sup>National Physical Laboratory, Teddington, United Kingdom

<sup>6</sup>King's College London, London, United Kingdom

<sup>7</sup>University of Surrey, Surrey, Guildford, United Kingdom

<sup>8</sup>School of Mathematics and Physics, University of Surrey,  
Guildford, United Kingdom

<sup>9</sup>Department of Public Health and Primary Care, University of  
Cambridge, Cambridge, United Kingdom

## Abstract

**Background:** Photoplethysmography (PPG) is a non-invasive physiological sensing method used in many clinical applications, increasingly supported by machine learning. However, systematic comparisons of input representations and models remain limited. **Methods:** We address this gap in the research landscape by a comprehensive benchmarking study covering three kinds of input representations, interpretable features, image representations and raw waveforms, across prototypical regression and classification use cases: blood pressure (BP) estimation and atrial fibrillation (AF) prediction. **Results:** In both cases, the best results are achieved by deep neural networks operating on raw time series as input representations. Within this model class, the strongest performance is observed for deeper convolutional neural networks (CNNs). However, depending on the task, smaller or lower-capacity CNNs can also achieve

competitive performance, as confirmed by Bland–Altman analyses and statistical significance analyses based on bootstrapping. **Conclusions:** By providing a controlled, like-for-like comparison across signal, feature, and image-based representations, this study offers practical guidance for selecting robust machine-learning approaches for real-world PPG applications.

**Keywords:** Photoplethysmography, Machine Learning, Deep Neural Networks, Blood Pressure Estimation, Atrial Fibrillation Detection.

## 1 Introduction

PPG is one of the most commonly used wearable sensing techniques. It consists of projecting light onto the skin and measuring the amount of light that is reflected back or transmitted through the underlying tissues. Its simplicity, non-invasive nature, and ability to deliver multiple physiological parameters make it particularly attractive [1, 2]. As a result, PPG has been integrated into a range of clinical devices, such as pulse oximeters, as well as consumer wearable devices, including smartwatches.

The PPG signal measures the fluctuations in blood volume in the skin’s microvascular bed, which occur with each heartbeat. Figure 1 shows an exemplary PPG signal: the shape of the pulse wave contains information relating to the heart and vasculature, including BP, and the inter-beat intervals are related to heart rhythm [3]. The time delay between the electrical activation of the heart and the arrival of the corresponding pulse wave at a peripheral site where PPG is measured has been used to predict BP. There are generally two approaches to analysing PPG signals [1]: (i) using signal processing to extract features relating to pulse wave shape or inter-beat-intervals; and (ii) using deep learning techniques to analyse PPG signals or their image-based representations. Over the past few years, deep learning techniques have become widely used [4, 5, 6], as they have often shown superior performance to feature-based approaches.

In the present study, we investigate two widely considered clinical applications for PPG analysis: AF classification as a prototypical classification task and cuffless BP estimation as a prototypical regression task. AF is the most common sustained cardiac arrhythmia and confers a five-fold increase in stroke risk [8]. AF is characterised by irregular and often very rapid heart rhythm. PPG provides an attractive approach to identifying AF because it is widely used in consumer wearables, and because it can detect each heartbeat, it can provide measures of the heart rhythm. During an AF episode, the time intervals between heartbeats are irregular. BP is one of the most widely used physiological measurements. It is a key marker of cardiovascular health; a valuable predictor of cardiovascular events; and is essential for the selection and monitoring of anti-hypertensive (BP lowering) treatments [9]. PPG-based BP estimation provides a potential approach to monitor BP unobtrusively in daily life. Accordingly, numerous studies have explored non-invasive and cuffless BP monitoring using

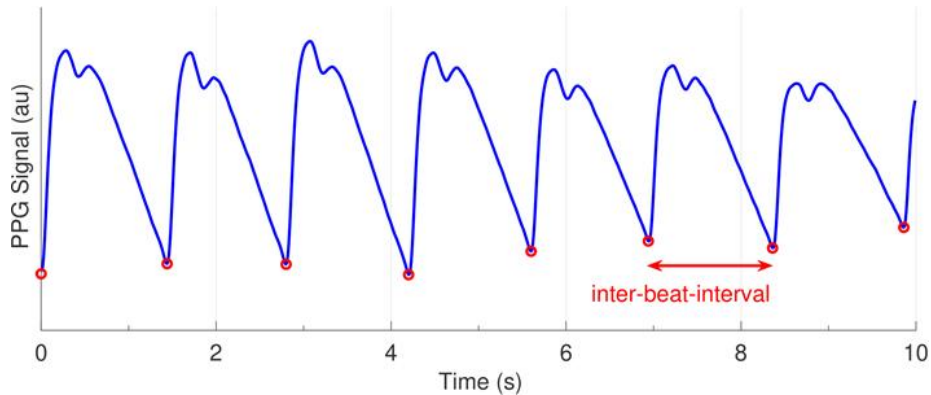


Figure 1: An exemplary PPG signal showing a pulse wave for each heartbeat. Pulse onsets, representing individual heartbeats, are shown as red circles. An inter-beat interval is labeled, corresponding to the time between consecutive heartbeats (adapted from [7]).

PPG and related physiological signals, spanning feature-based methods as well as deep learning approaches [5, 6]. The rationale behind selecting two prototypical, but very different use cases, is to identify general patterns that could guide practitioners in the field even beyond the two investigated use cases.

While many prediction models have been put forward for the two considered prediction tasks at hand, benchmarking results are typically presented within a set of prediction models operating on a single kind of input modality, or a comparison is carried out against previously reported results from the literature. However, the latter relies on matching the experimental setup as closely as possible, where deviations from this setup severely limits the comparability of the results. The current lack of directly comparable benchmarking is an important gap in the research landscape, which we aim to address with this submission. This lack of controlled, directly comparable benchmarking across input representations and model families motivates the present study.

In this work, we address the following research questions: How do state-of-the-art machine learning models operating on different inputs representations compare? Are there universal patterns in terms of best-performing input representations or model architectures across different prototypical classification and regression use cases? As our main technical contribution, we put forward a like-for-like benchmarking of a comprehensive set of state-of-the-art algorithms covering three kinds of input representations on two large-scale datasets for a prototypical classification task (AF classification) and two different variants of a prototypical regression task (BP regression), using identical data splits and evaluation protocols to enable direct comparison across model families and to identify robust performance patterns that generalize beyond a single model or dataset.

## 2 Related Work

**Overview of Learning Paradigms for PPG Analysis.** To clarify the structure of this section, we organize prior work primarily by the input representation used for PPG analysis rather than by the learning algorithm. Specifically, we distinguish between models operating on raw time-series signals, engineered or clinically interpretable features, and image-based representations. While similar architectures (e.g., CNNs or RNNs) may appear across categories, the defining criterion is the form of the input representation. Typically, all approaches for clinical prediction tasks based on PPG data rely on a combination of signal processing and machine learning, where the precise focus varies considerably across different approaches. At one end of the spectrum, approaches relying on clinically interpretable features focus heavily on signal processing to extract meaningful features, and typically use comparably simple classification/regression models to perform the prediction. At the other end of the spectrum, deep learning methods using raw time series as input with as little signal processing as possible, rely on complex prediction models to extract and process meaningful features by themselves. In between, there are classifiers based on image-representations, that leverage signal processing tools to turn raw waveforms into image representations, and then most commonly also rely on deep learning models to perform the prediction.

**Raw Time Series as Input Representations.** Recent advancements in deep learning have significantly impacted healthcare by enabling complicated analysis of raw physiological data. These models are particularly effective in estimating BP and detecting AF, among other applications. The key advantage of deep learning is its ability to recognize complicated patterns directly from raw data such as electrocardiogram (ECG) and PPG signals, eliminating the need for extensive manual feature development [10, 11, 12]. They provide an effective means to learn the complex, nonlinear underlying relationship between PPG signals and various physiological parameters, without the need to define a convenient analytical form for such a transformation. Consequently, deep learning architectures such as convolutional neural networks (CNNs) and recurrent neural networks (RNNs) have shown remarkable performance in BP estimation, by capturing the temporal and spatial nuances inherent in raw physiological signals [13]. Very recent work also demonstrated strong performance of hybrid CNN-BiLSTM architectures with attention on large datasets [14].

Similarly, deep learning models have demonstrated significant potential in detecting AF from raw ECG signals. The authors of [11] developed a deep learning model employing a CNN to detect AF from single-lead ECG recordings. Their model demonstrated high accuracy, underscoring the potential of deep learning in the detection of arrhythmias. Similarly, [15, 16, 17] implemented deep learning approaches using CNNs on PPG signals for AF detection. These approaches yielded results that were competitive with ECG-based methods, thereby demonstrating the feasibility of utilizing PPG signals for AF detection. End-to-end deep learning frameworks that process raw ECG data to generate AF predictions

have simplified and improved the accuracy of AF detection.

Beyond PPG-specific investigations, several prior works [18, 19] have put forward benchmarks on a diverse set of time series classification tasks, establishing, for example, InceptionTime and MiniRocket as robust baselines models, which encourage their use in PPG-based prediction tasks.

More recently, transformer-based architectures have been explored for PPG and other physiological time-series analysis. Several studies have reported competitive performance of Transformer or hybrid CNN–Transformer models for time series forecasting [20, 21]. However, their effectiveness relative to convolutional architectures remains task- and data-dependent [22].

**Feature-Based Input Representations.** Besides working on raw data, another possibility to solve classification or regression tasks on PPG data is to establish machine learning models operating on clinically interpretable PPG features. This includes features based on pulse morphology, e.g., PPG pulse wave features such as the systolic peak, the diastolic peak or pulse duration, and PPG derivative features [5, 23], and irregularity features based on measures of randomness, variability and complexity in the inter-beat-intervals that can be determined from the PPG [24, 25]. These clinically interpretable PPG features are used for BP estimation (see below), AF detection (see below), and other questions related to the cardiovascular system, e.g. the assessment of arterial stiffness [26]. In addition, PPG signals sometimes show a strict periodic behaviour or, in general, a quasi-periodic behaviour. This motivates the use of features from Fourier- [27], Wavelet- [28] or Hilbert-Huang- [29] Transformations for training models. Such models are defined for BP estimation and AF detection. In related work, features from Fourier-Transformation are used to define models for the detection of aneurysms [30] or stenoses [31]. As PPG signals are in general not periodic, but quasiperiodic, one might expect better results with Wavelet- or Hilbert-Huang-transformations.

**Image-Based Input Representations.** Image-based models, such as those using the Continuous Wavelet Transform (CWT) or short-time Fourier transform (STFT), convert physiological signals into visual representations, enabling deep learning to analyze, classify, and estimate physiological parameters.

The CWT is a powerful tool for analyzing localized variations of power within a time series signal. Unlike the Fourier Transform, which provides a global frequency representation, CWT can provide a time-frequency representation that preserves the temporal localization of features. CWT-based scalograms have been used for PPG signal transformation to classify BP (Normal, Prehypertension, Stage 1 hypertension, and Stage 2 hypertension) [32, 33], estimate heart rate variability (HRV) and signal quality [34] as well as to detect AF [16]. CWT’s scale-adaptive time–frequency resolution suits PPG’s non-stationary, multi-scale nature, and its rich scalograms representation consistently delivers strong performance across various tasks.

The STFT-based spectrogram representation has been used in several PPG-

based predictions using DL [35, 35]. In this approach, the PPG signals were transformed into fixed-resolution time–frequency spectrograms using the STFT and processed using a ResNet architecture. This approach, Spectrogram-ResNet, makes it possible to use the image-based convolutional neural networks by using a simpler time–frequency representation compared to the CWT process [35]. The standard STFT approach was also used in [35] for signal quality estimation.

Several alternatives have been explored for image-based PPG representations [16, 33]. These include direct conversion of the 1D PPG waveform into a structured 2D representation (e.g. multi-channel raw-PPG derivatives obtained by stacking padded PPG cycles (or beats)) which has also been applied for BP estimation [36], Gramian Angular Fields (GASF/GADF) [37] to encode temporal correlations, Visibility Graphs [38] providing a topological view of waveform structure, and Symmetric Projection Attractor Reconstruction (SPAR) attractor images which encapsulate the morphology and variability of the signal [39, 40]. The optimal choice depends on the downstream task, as each method has distinct strengths and limitations.

## 3 Materials and Methods

### 3.1 Datasets

This study utilized the PPG data contained in the VitalDB dataset [41] for BP estimation and in the DeepBeat dataset [42] for the AF detection task.

**VitalDB dataset.** The VitalDB dataset includes ECG, PPG, and invasive arterial blood pressure (ABP) signals collected using patient monitors from surgical patients [43]. Wang et al. [41] published the pre-processed VitalDB dataset as a subset of the PulseDB dataset, from which we use the PPG signals of 10s length with a sampling frequency of 125 Hz, and reference systolic BP (SBP) and diastolic BP (DBP) values derived from the ABP signals. We used the VitalDB subset instead of the entire PulseDB dataset as it reduced the dataset size and was shown to lead to good generalization to out-of-distribution data [44].

The dataset supports both calibration-based and calibration-free evaluation protocols for assessing BP model generalizability, where calibration denotes subject-specific adaptation using reference BP measurements without retraining or fine-tuning the model, through samples from the same subject in the training and test sets following the PulseDB convention [41]. This differs from the calibration definitions used in some prior cuffless BP studies (e.g., [45]), where calibration may involve explicit model adaptation or fine-tuning. The calibration-free scenario ensures no patient overlap between training and test set and therefore assesses the generalization to unseen patients.

We refer to the first scenario as **VitalDB ‘Calib’** and to the second scenario

as **VitalDB ‘CalibFree’**. To ensure comparability with literature results, we keep the original test sets intact but split the original training sets into training, validation, and calibration sets, where the latter is not considered in this study, mimicking the way the respective test sets were created, i.e., defining validation sets with/without patient overlap for VitalDB ‘Calib’/‘CalibFree’. In Table 1, we summarize the two considered subsets, where one sample corresponds to a segment of 10s length.

Subset	VitalDB ‘Calib’	VitalDB ‘CalibFree’
Train (samples / subjects)	418986 / 1293	416880 / 1158
Validation (samples / subjects)	40673 / 1293	32400 / 90
Test (samples / subjects)	51720 / 1293	57600 / 144
Age (years, mean $\pm$ SD)	58.9 $\pm$ 15.0	58.8 $\pm$ 15.0
Sex (M%)	57.6	57.9
SBP (mmHg, mean $\pm$ SD)	115.4 $\pm$ 18.9	115.4 $\pm$ 18.9
DBP (mmHg, mean $\pm$ SD)	62.9 $\pm$ 12.0	62.9 $\pm$ 12.0

Table 1: Characteristics of the VitalDB subsets used for BP estimation.

**DeepBeat dataset.** For the AF classification task, we leverage the DeepBeat dataset [42]. The dataset comprises more than 500,000 25-second, 32 Hz PPG segments, henceforth referred to as samples, from 175 individuals (108 with AF, 67 without). PPG signals were collected using a wrist-based PPG wearable device from cohorts of participants before cardioversion, patients undergoing an exercise stress test, and during daily life [42]. In the original publication [42], due to an uneven AF/non-AF distribution across splits, performance metrics were overestimated, and the strong test scores did not reflect equivalent success on the validation and training sets. To address these issues, we implement a new data split. We ensure no overlap between sets by redistributing subjects, thereby eliminating the redundancy present in the original dataset (Table 2). This revised split maintains an equal AF/non-AF ratio across the training, validation, and test sets, thus providing a more reliable representation and enhancing the robustness of our model evaluation. (For more details, please refer to the Supplementary Material.)

Dataset	DeepBeat (AF classification)			
	AF	Non-AF	Data Ratio	AF Ratio
Train (samples / subjects)	40603 / 50	65646 / 38	0.78	0.38

Dataset	DeepBeat (AF classification)			
Subset	AF	Non-AF	Data Ratio	AF Ratio
Validation (samples / subjects)	5800 / 19	9456 / 7	0.11	0.38
Test (samples / subjects)	5797 / 19	9580 / 5	0.11	0.37

Table 2: Characteristics of the DeepBeat subsets used for AF classification. “Data Ratio” indicates the proportion of the full dataset assigned to each subset, and “AF Ratio” denotes the fraction of samples within that subset labeled as AF.

### 3.2 Performance Evaluation and Metrics

To keep the main text concise, we summarize our evaluation methods here. For a detailed explanation of the procedures and metrics used, please refer to the Supplementary Material.

**BP Estimation.** We evaluate BP predictions using the Mean Absolute Error (MAE) and Mean Absolute Scaled Error (MASE), comparing model outputs against a baseline that predicts the training set median. Metrics are reported separately for systolic and diastolic pressures.

Furthermore, to determine the agreement between predictions and reference values in more detail, Bland-Altman analyses were also performed [46]. The bias was determined as the mean difference between predictions and reference values, as well as the corresponding limits of agreement (LoA). The standard deviation of these differences was multiplied by 1.96 to determine the LoA. While MAE roughly indicates the size of errors, bias directly indicates systematic errors, while the LoA gives insight into the variability of individual prediction errors.

We also provide the grading (A, B, C, D) based on IEEE 1708a-2019 standard [47] which are calculated based on the difference between the device or model’s BP predictions and the reference (cuff-based) measurements;

- **Grade A:** Errors  $\leq 5$  mmHg
- **Grade B:** Errors  $> 5$  mmHg and  $\leq 6$  mmHg
- **Grade C:** Errors  $> 6$  mmHg and  $\leq 7$  mmHg
- **Grade D:** Errors  $> 7$  mmHg

We acknowledge that there are other BP estimation standards such as AAMI [48] and BHS [49]. In this manuscript, however, we restrict ourselves to the IEEE

standard and defer a detailed comparison according to different BP estimation standards to future work.

**AF Detection.** AF detection performance is assessed using standard metrics: sensitivity, specificity, receiver operator characteristic (ROC) area under the curve (AUC), F1 score, and Matthews correlation coefficient (MCC). Classification thresholds are adjusted to meet desired sensitivity/specificity criteria, with a default threshold of 0.5 for the F1 score and optimized thresholds for other metrics. We explore two different threshold choices by fixing the threshold such that either sensitivity or specificity exceeds 0.8.

**Statistical significance.** For every experimental setting, the best model, defined as the model with the lowest MAE for the regression tasks or the highest AUC for the classification tasks, was taken as the reference model. We then computed the performance difference between the reference model and every other model by performing 1,000 bootstraps. A performance difference whose 95% confidence interval did not contain zero indicated a model to be statistically significantly worse. Conversely, if zero was in the interval, then the method indicated that the respective model was not statistically significantly worse than the reference, which was indicated in the result tables accordingly.

### 3.3 Prediction models

In our study, we explore the use of three different input representations – time series, feature-based, and image-based approaches – each providing unique advantages in capturing the underlying physiological information. We consider several architectures, each designed to process either raw signals, extracted features, or visual representations to accurately estimate BP values and classify heart rhythms. All models were trained from scratch. The learning rate, as the most important hyperparameter, was systematically optimized based on the validation set performance, while model-dependent hyperparameters were deliberately not extensively tuned to preserve a balanced experimental setting. Due to the large number of considered model architectures, a more systematic exploration of hyperparameter choices was considered infeasible given the computational resources available for this study. Retrospectively, we see rather comparable performance levels across different input representations and involving independent code bases as an indication that the models/hyperparameter choices were not suboptimal.

**Baseline Models.** On VitalDB CalibFree, the baseline model (used for BP estimation) predicts BP by outputting the median SBP/DBP value of the BP data inferred from the training set for any given input, providing a straightforward reference for evaluating the performance of more advanced predictive models. On VitalDB Calib, we use The subject-specific median was calculated as the prediction on the test set.

**Raw Time Series Models.** For both BP estimation and AF detection, deep learning architectures such as CNNs, RNNs, and temporal convolutional net-

works (TCNs) have been used to process raw ECG or PPG sequences to capture complex temporal patterns, directly predicting continuous values for regression or output probabilities for classification. The specific models used in this study were:

- **LeNet1d:** A one-dimensional CNN adapted from the original LeNet architecture for feature extraction from raw ECG/PPG time-series data [50].
- **Inception1d:** A 1D adaptation of the Inception architecture that uses parallel convolutional layers to capture multi-scale temporal features [18].
- **XResNet1d50/101:** Deep residual networks modified for 1D data, incorporating group normalization and selective kernel sizes to learn hierarchical features from physiological signals [51].
- **XResNet1d50+GNLL:** This case uses the XResNet50d model with a Gaussian Negative Log Likelihood Loss (GNLL) instead of the conventional MAE loss as proposed in [52].
- **AlexNet1d:** A one-dimensional variant of AlexNet that processes time series data through convolutional and pooling layers for regression and classification tasks [53].
- **MiniRocket:** A nearly deterministic transform using dilated convolutions and a linear classifier, offering fast and effective feature extraction from time-series data [19].
- **Temporal Convolutional Networks (TCNs):** Networks using dilated causal convolutions and residual connections to capture long-range dependencies in sequential physiological signals [54].
- **PPNet:** A hybrid architecture consisting of CNN and LSTM layers designed to extract spatial and temporal representations from physiological time series [55].
- **iTransformer:** A transformer-based model tailored for time series prediction and analysis for instance-specific normalization techniques and attention mechanisms for improved sequence modelling [21].
- **TimesNet:** A convolutional inception-like architecture for time series analysis which uses multi-periodic modelling by convolutional blocks for extracting detailed temporal patterns [20].

We can roughly categorize the considered models into complex/deep models (Inception1D, XResNet1d50, XResNet1d101, AlexNet1d, TCNs ) and simple/shallow models (LeNet1d, MiniRocket).

**Feature-Based Models.** Clinically interpretable features are extracted from PPG signals, such as pulse morphology metrics for BP estimation and irregularity measures for AF detection, and fed into machine learning algorithms to perform regression or classification tasks with clearer interpretability. The specific models and techniques used in this study were:

- **Clinically interpretable features (CIF):** CIF for BP includes features such as systolic peaks, diastolic peaks, pulse duration, and pulse morphology metrics [56]. These features reflect vascular health, haemodynamic dynamics, and arterial compliance, making them well-suited for modelling BP. CIF for AF comprises features related to rhythm irregularity, such as randomness [57], variability [58, 59], and complexity in inter-beat-intervals [60]. These features highlight the irregular heart rhythms characteristic of AF. Table 3 provides an overview of the hand-crafted features used in the feature-based models. The full list of features is described in the supplementary material. These features are combined with the following prediction models:
  - **Multi-layer perceptron (MLP):** An MLP is a fully connected feedforward neural network that maps input features to target outputs through multiple layers of neurons.
  - **Gaussian Process Regression (GPR):** A non-parametric regression method that models complex relationships between PPG features and BP, providing probabilistic predictions [61].
- **Wavelet Transformation:** A Wavelet-based method such as Wavelet Packet Decomposition using the Discrete Wavelet Transform [62] is applied to the raw PPG signal. This transformation decomposes the signal into time-frequency components, extracting features that capture both transient and long-term patterns in the data. It should be noted that Wavelet + MLP forms a pipeline where the wavelet transform serves as a sophisticated feature extractor, and the MLP functions as the predictive model utilizing those features.

It should be noted that only the CIF directly reflects physiological mechanisms, e.g. pulse morphology or rhythm irregularity. On the other hand, features derived from mathematical transformations (e.g., wavelet coefficients) provide useful signal representations; however, they are not directly interpretable in clinical terms.

**Image-Based Models:** One-dimensional signals can be converted into two-dimensional images, which capture the essence of the signal in a compact domain. Traditional image recognition CNNs can then be used with these image inputs. There are many different ways of converting signals to images, but this study only used the following two approaches:

- **Continuous Wavelet Transform (CWT) Scalograms:** PPG signals are transformed into time-frequency images derived from PPG signals that capture localized signal variations [32]. The CWT-based images are used as inputs for ResNet18 models [63].
- **STFT-Based Spectrograms (Spectrogram-ResNet):** PPG signals are transformed into fixed-resolution time-frequency spectrograms using the STFT [35]. The resulting spectrograms are processed using convolu-

Table 3: Overview of feature categories and corresponding feature-based pipelines used for BP estimation and AF detection.

Pipeline	Feature category	BP	AF	Description / Examples
CIF	Time-domain morphology		–	Pulse amplitude, rise time, decay time, pulse duration, area under the pulse
CIF	Derivative-based		–	First and second derivative extrema, slope-based indices
CIF	Temporal variability	–		Inter-beat intervals (PP intervals), HR, HRV, rhythm irregularity measures
CIF	Frequency-domain	–		Spectral power in predefined frequency bands capturing rhythm variability
CIF	Quality-related			Signal quality indices, beat consistency measures
Wavelet + MLP	Wavelet-based features			Wavelet packet decomposition coefficients used as task-agnostic feature representations

tional neural network architectures based on ResNet-50 and ResNet-18, initialized with ImageNet pre-trained weights [64, 65].

Table 10 lists overall parameter counts of all models within the tasks of AF detection and BP estimation, and is condensed by input representation (T/F/I). It is worth noting that parameter count is reported as a coarse, hardware-agnostic indicator of model complexity and is used in this work as a relative measure of computational efficiency, but should not be interpreted as a direct proxy for deployment cost on wearable or embedded hardware, where inference latency, memory footprint, and energy consumption are strongly platform dependent. For more details on these models and their implementations, please see the Supplementary Material.

## 4 Results

### 4.1 BP Estimation

Tables 4, 5, 6, and 7 display the results of BP (SBP/DBP) prediction using different deep learning models based on VitalDB Calib and VitalDB CalibFree datasets, respectively. The baseline models achieved MAEs of 14.87 and 9.43 mmHg for SBP and DBP, respectively, on CalibFree, and 10.72 and 5.78 mmHg, respectively, on Calib. On Calib, the per-subject baseline performed substantially better than the global baseline (10.72 and 5.78 mmHg vs. 14.91 and 9.52 mmHg respectively).

Model performance varied between models and tasks. On CalibFree, almost all

models provided an improvement over baseline for both SBP and DBP (the only exception being the Inception1d SBP model). However, the level of improvement was moderate at best, with the lowest MASEs of 0.83 for both SBP and DBP achieved by XResNet1d50, indicating 17% reductions in MAE in comparison to baseline. This resulted in at best 26% of SBP estimates and 40% of DBP estimates falling into the top grade (i.e. errors  $\leq 5$  mmHg). On Calib, there was greater variation in model performances, with XResNet1d50+GNLL achieving the lowest MASEs of 0.73 and 0.87 for SBP and DBP, respectively, corresponding to 48% of SBP estimates and 64% of DBP estimates falling into the top grade. In contrast, several models performed worse than the per-subject baseline, with the worst-performing model, CIF+MLP, achieving MASEs of 1.27 and 1.54 for SBP and DBP, respectively. Indeed, for DBP estimation, only the XResNet1d50+GNLL model achieved an improvement over the subject-specific baseline, whereas all others performed worse than this baseline. Absolute performance in terms of MAE was better on Calib than CalibFree, as shown by lower MAEs on Calib than CalibFree for all models except the TCN+MLP SBP and DBP models, and the CIF+MLP DBP model. MLP models always performed worse than other models of the same type.

Model	SBP			IEEE Grades (SBP)			
	MAE (MASE)	Bias	LoA	A	B	C	D
<b>B</b> Baseline (global)	14.91 (1.39)	0.00	36.94	0.21	0.04	0.04	0.71
Baseline (per subject)	10.72 (1.00)	0.00	28.01	0.34	0.06	0.05	0.55
XResNet1d101	9.06 (0.84)	0.25	24.51	0.40	0.06	0.06	0.48
XResNet1d50	9.52 (0.88)	0.29	25.00	0.37	0.06	0.06	0.51
<b>T</b> Inception1d	9.43 (0.88)	-0.90	24.55	0.36	0.06	0.06	0.52
LeNet1d	11.76 (1.09)	-0.78	29.40	0.27	0.05	0.05	0.63
XResNet1d50+GNLL	<b>7.99</b> <b>(0.74)</b>	-0.79	22.44	0.48	0.06	0.05	0.41
AlexNet1d	9.49 (0.88)	-0.54	25.21	0.38	0.06	0.06	0.50
Minirocket	11.24 (1.05)	0.11	28.39	0.29	0.06	0.05	0.60
iTransformer	12.66 (1.18)	-0.35	31.71	0.25	0.05	0.05	0.65
TimesNet	12.69 (1.16)	-0.71	31.88	0.25	0.05	0.05	0.65

Model	SBP			IEEE Grades (SBP)				
	MAE (MASE)	Bias	LoA	A	B	C	D	
PPNet	<b>8.76</b> (0.81)	-0.42	<b>23.63</b>	0.41	0.06	0.06	0.47	
TCN +MLP	<b>12.84</b> (1.19)	-5.50	<b>30.71</b>	0.25	0.05	0.05	0.65	
<b>F</b>	WAVELET	<b>13.62</b> (1.26)	-1.77	<b>34.10</b>	0.24	0.05	0.04	0.67
	+MLP	<b>12.22</b> (1.13)	-0.32	<b>32.03</b>	0.27	0.05	0.05	0.63
	CIF +GPR	<b>13.78</b> (1.27)	-0.13	<b>34.21</b>	0.23	0.04	0.04	0.69
	CIF +MLP	<b>13.78</b> (1.27)	-0.13	<b>34.21</b>	0.23	0.04	0.04	0.69
<b>I</b>	CWT	<b>10.91</b> (1.01)	-0.24	<b>28.51</b>	0.32	0.06	0.05	0.57
	Spectrogram-ResNet-18	<b>9.85</b> (0.91)	-1.14	<b>26.83</b>	0.38	0.06	0.06	0.50
	Spectrogram-ResNet-50	<b>9.82</b> (0.91)	-0.81	<b>26.88</b>	0.39	0.06	0.06	0.49

Table 4: The SBP performance on the VitalDB Calib dataset for three input representations, T for raw time series, F for feature-based, and I for image-based models, next to B for the baseline model. The best-performing model is marked in bold and underlined. Models that do not perform statistically significantly worse than the best model are shown in bold. All MAE values are given in units of mmHg. Bias and LoA were computed following Bland–Altman analysis (bias  $\pm$  1.96 SD).

Model	DBP			IEEE Grades (DBP)				
	MAE (MASE)	Bias	LoA	A	B	C	D	
<b>B</b>	Baseline (global)	<b>9.52</b> (1.65)	0.00	<b>23.66</b>	0.32	0.06	0.06	0.56
	Baseline (per subject)	<b>5.78</b> (1.00)	0.00	<b>15.37</b>	0.56	0.07	0.06	0.30
	XResNet1d101	<b>5.91</b> (1.02)	-0.06	<b>15.86</b>	0.55	0.07	0.06	0.32
	XResNet1d50	<b>6.33</b> (1.08)	0.02	<b>16.51</b>	0.50	0.08	0.07	0.35
<b>T</b>	Inception1d	<b>6.37</b> (1.11)	-0.02	<b>16.46</b>	0.50	0.07	0.07	0.36

Model	DBP			IEEE Grades (DBP)			
	MAE (MASE)	Bias	LoA	A	B	C	D
LeNet1d	7.80 (1.35)	1.00	19.34	0.39	0.07	0.07	0.47
XResNet1d50 +GNLL	<b><u>5.09</u></b> <b><u>(0.87)</u></b>	-0.52	14.56	0.64	0.06	0.05	0.25
AlexNet1d	6.10 (1.05)	-0.14	16.33	0.54	0.07	0.06	0.33
Minirocket	7.33 (1.26)	0.01	18.51	0.43	0.07	0.07	0.43
iTransformer	8.20 (1.41)	-0.18	20.53	0.38	0.07	0.06	0.49
TimesNet	8.12 (1.40)	0.01	20.69	0.38	0.07	0.06	0.49
PPNet	5.58 (1.01)	-0.18	15.23	0.58	0.07	0.06	0.29
TCN +MLP	8.48 (1.46)	-3.12	20.46	0.37	0.07	0.07	0.49
<b>F</b> WAVELET +MLP	8.84 (1.51)	-1.00	22.08	0.36	0.07	0.06	0.51
CIF +GPR	7.78 (1.35)	-0.10	19.69	0.40	0.07	0.07	0.46
CIF +MLP	8.94 (1.54)	-0.55	22.18	0.35	0.06	0.06	0.53
<b>I</b> CWT	6.68 (1.15)	-0.32	17.66	0.50	0.07	0.06	0.37
Spectrogram- ResNet-18	6.33 (1.09)	-0.64	17.21	0.54	0.07	0.06	0.33
Spectrogram- ResNet-50	6.39 (1.10)	-0.10	17.42	0.53	0.07	0.06	0.34

Table 5: The DBP performance on the VitalDB Calib dataset for three input representations, T for raw time series, F for feature-based, and I for image-based models, next to B for the baseline model. The best-performing model is marked in bold and underlined. Models that do not perform statistically significantly worse than the best model are shown in bold. All MAE values are given in units of mmHg. Bias and LoA were computed following Bland–Altman analysis (bias  $\pm$  1.96 SD).

	Model	SBP			IEEE Grades (SBP)			
		MAE (MASE)	Bias	LoA	A	B	C	D
<b>B</b>	Baseline	14.87 (1.00)	-0.00	36.94	0.21	0.04	0.04	0.71
<b>T</b>	XResNet1d101	12.43 (0.83)	-1.28	30.91	0.25	0.05	0.05	0.65
	XResNet1d50	12.46 (0.83)	-0.23	31.09	0.24	0.05	0.05	0.66
	Inception1d	14.46 (0.97)	-3.15	30.62	0.25	0.05	0.05	0.65
	LeNet1d	12.37 (0.83)	0.86	30.57	0.25	0.05	0.05	0.65
	XResNet1d50+GNLL	<b>12.27</b> <b>(0.82)</b>	-0.99	30.55	0.26	0.05	0.05	0.64
	AlexNet1d	12.51 (0.84)	0.52	31.24	0.25	0.05	0.05	0.65
	Minirocket	12.65 (0.85)	-0.95	31.43	0.26	0.05	0.05	0.64
	iTransformer	13.15 (0.88)	-0.75	32.76	0.24	0.05	0.05	0.66
	TimesNet	13.09 (0.88)	-1.89	32.84	0.25	0.05	0.05	0.65
	PPNet	12.56 (0.84)	-2.05	31.24	0.25	0.05	0.05	0.65
	TCN +MLP	12.72 (0.85)	-2.52	31.77	0.25	0.05	0.05	0.65
	<b>F</b>	WAVELET +MLP	14.21 (0.95)	0.03	35.32	0.22	0.04	0.04
CIF +GPR		12.90 (0.87)	-0.32	32.38	0.25	0.05	0.04	0.66
CIF +MLP		14.02 (0.94)	0.15	34.82	0.24	0.04	0.04	0.68
<b>I</b>	CWT	13.49 (0.90)	-1.14	33.63	0.23	0.05	0.04	0.68
	Spectrogram- ResNet-18	13.01 (0.87)	0.32	32.29	0.24	0.04	0.04	0.68
	Spectrogram- ResNet-50	13.53 (0.90)	3.40	32.88	0.24	0.04	0.04	0.68

Model	SBP			IEEE Grades (SBP)			
	MAE (MASE)	Bias	LoA	A	B	C	D

Table 6: The SBP performance on the VitalDB CalibFree dataset for three input representations, T for raw time series, F for feature-based, and I for image-based models, next to B for the baseline model. The best-performing model is marked in bold and underlined. Models that do not perform statistically significantly worse than the best model are shown in bold. All MAE values are given in units of mmHg. Bias and LoA were computed following Bland–Altman analysis (bias  $\pm$  1.96 SD).

Model	DBP			IEEE Grades (DBP)			
	MAE (MASE)	Bias	LoA	A	B	C	D
<b>B</b> Baseline	9.43 (1.00)	0.00	23.66	0.33	0.06	0.06	0.55
XResNet1d101	<b>7.93</b> <b>(0.84)</b>	0.18	19.70	0.39	0.07	0.06	0.48
XResNet1d50	7.98 (0.84)	-1.55	19.63	0.39	0.07	0.06	0.48
Inception1d	<b>7.94</b> <b>(0.84)</b>	-1.86	19.29	0.38	0.07	0.06	0.49
<b>T</b> LeNet1d	<b>7.92</b> <b>(0.84)</b>	1.26	19.45	0.39	0.07	0.06	0.48
XResNet1d50+GNLL	<b>7.94</b> <b>(0.84)</b>	-0.54	19.63	0.39	0.07	0.06	0.48
AlexNet1d	7.98 (0.84)	0.15	19.80	0.38	0.07	0.07	0.48
Minirocket	8.08 (0.85)	-1.01	19.87	0.38	0.07	0.06	0.49
iTransformer	8.37 (0.88)	-0.67	20.77	0.37	0.07	0.06	0.50
TimesNet	8.29 (0.87)	-0.71	20.79	0.38	0.07	0.06	0.49
PPNet	<b>7.95</b> <b>(0.84)</b>	-0.91	19.74	0.39	0.07	0.07	0.48
TCN +MLP	8.24 (0.87)	-1.77	20.27	0.38	0.06	0.06	0.50
<b>F</b> WAVELET +MLP	8.89 (0.94)	-0.78	22.10	0.35	0.06	0.06	0.53

Model	DBP			IEEE Grades (DBP)			
	MAE (MASE)	Bias	LoA	A	B	C	D
CIF +GPR	8.15 (0.86)	-0.44	20.41	0.38	0.07	0.06	0.49
CIF +MLP	8.69 (0.92)	0.38	21.61	0.36	0.06	0.06	0.52
CWT	8.41 (0.89)	-0.18	20.96	0.37	0.07	0.07	0.49
<b>I</b> Spectrogram- ResNet-18	8.04 (0.85)	0.27	19.92	0.38	0.07	0.07	0.48
Spectrogram- ResNet-50	8.34 (0.88)	2.00	20.30	0.37	0.07	0.06	0.50

Table 7: The DBP performance on the VitalDB CalibFree dataset for three input representations, T for raw time series, F for feature-based, and I for image-based models, next to B for the baseline model. The best-performing model is marked in bold and underlined. Models that do not perform statistically significantly worse than the best model are shown in bold. All MAE values are given in units of mmHg. Bias and LoA were computed following Bland–Altman analysis (bias  $\pm$  1.96 SD).

Raw time series (T) and image-based (I) models performed better than feature-based (F) models on Calib (with the one exception of TCN+MLP), as shown by MASEs of 0.73-1.07 (SBP) and 0.87-1.46 (DBP) for raw time series and image-based models, compared to 1.13-1.27 and 1.35-1.54 for feature-based models. There was a less clear difference in performance on CalibFree. Whilst best performance was achieved with raw time series models, the image-based model performed better than three raw time series models on Calib, and better than one raw time series model on CalibFree. For Calib, more complex models seem to exhibit an advantage (comparing, for example, XResNet1d50 and XResNet1d101), most likely due to the ability to memorize subject-specific signal patterns. The only exception from this pattern seems to be the AlexNet1d model, which shows a performance that is almost on par with more complex models and considerably better than comparable lightweight models (such as LeNet1d or TCN+MLP).

Absolute performance in terms of MAE was always better for DBP estimation than for SBP estimation. However, when considering errors relative to baseline, MASEs were broadly similar between SBP and DBP on CalibFree, and always higher for DBP than SBP on Calib. Since the IEEE grading system uses absolute errors, performance in terms of IEEE Grades was generally better for DBP than SBP.

## 4.2 AF Detection

Table 8 represents the performance analysis of the classification task (AF/ non-AF) based on the Deepbeat dataset. Specificity (sensitivity  $\geq 0.8$ ) and sensitivity (specificity  $\geq 0.8$ ) are reported at operating thresholds selected to ensure a minimum sensitivity or specificity of 0.8, respectively.

Similar to the regression task, raw time series (T) and image-based (I) models performed better than feature-based (F) models in all cases except for the LeNet1d raw time series model, which performed poorly. The best-performing models were Inception1d and XResNet1d50, which achieved AUCs of 0.87, and F1 scores of 0.72 and 0.69 respectively. As with the regression task, whilst best performance was achieved with the more complex raw time series models, the image-based model performed better than some raw time series models. Whilst feature-based models generally performed worst, wavelet-based features produced better performance than clinically interpretable features.

	Model	AUC	F1 (0.5)	Specificity (sensitivity > 0.8)	Sensitivity (specificity > 0.8)	MCC (sensi- tivity > 0.8)	MCC (speci- ficity > 0.8)
<b>T</b>	XResNet1d101	<b><u>0.85</u></b>	0.66	0.74	0.74	0.53	0.53
	XResNet1d50	<b><u>0.85</u></b>	0.69	0.75	0.74	0.54	0.54
	Inception1d	<b><u>0.85</u></b>	0.69	0.74	0.73	0.52	0.52
	LeNet1d	0.74	0.55	0.55	0.48	0.34	0.30
	AlexNet1d	0.82	0.65	0.68	0.65	0.46	0.45
	Minirocket	0.82	0.66	0.69	0.67	0.47	0.47
	iTransformer	0.68	0.40	0.47	0.36	0.27	0.17
	TimesNet	0.79	0.58	0.61	0.57	0.40	0.38
	PPNet	<b><u>0.85</u></b>	0.69	0.76	0.75	0.54	0.54
	TCN+MLP	<b><u>0.85</u></b>	0.67	0.75	0.74	0.54	0.53
<b>F</b>	WAVELET + MLP	0.76	0.60	0.58	0.52	0.37	0.33
	CIF+MLP	0.52	0.39	0.20	0.31	-0.002	0.13
<b>I</b>	CWT	0.82	0.69	0.72	0.69	0.50	0.49
	Spectrogram- ResNet-18	0.82	0.68	0.68	0.61	0.47	0.42
	Spectrogram- ResNet-50	<b><u>0.85</u></b>	0.69	0.72	0.69	0.50	0.49

Table 8: The performance analysis for the classification task on the DeepBeat dataset for three input representations: **T** for raw time series, **F** for feature-based, and **I** for image-based models. The best-performing model is marked in bold and underlined. Models that do not perform statistically significantly worse than the best model are shown in bold.

## 5 Discussion

### 5.1 BP Estimation

**Relative Performance Comparison.** For both regression tasks, the best results were achieved by approaches based on raw time series. Feature-based approaches were not competitive in the Calib scenario, but are to a certain degree competitive in the CalibFree scenario. Here, it is important to note the differences between Calib and CalibFree: CalibFree tests on unseen patients, whereas Calib purposely tests on patients already seen during training, i.e., . models can profit from a certain degree of memorization. Quite naturally, models achieved much better scores in the Calib setting (even though test sets are not entirely comparable). This also impacts the best-forming models in each of the two settings (within the category of models operating on raw time series). Large and complex models (such as XResNet1d and Inception1d) performed best on Calib, as overfitting to specific patients is desirable, whereas smaller models (such as LeNet1d) performed on par or even better than more complex models in the CalibFree scenario, where generalization to unseen patients is key. This observation aligns with the fact that the gap between raw time series and feature-based approaches is larger in the case of Calib, which is quite natural as this task largely profits from the complexity of the model (and all feature-based approaches are less complex than typical models operating on raw time series). Beyond aggregate error metrics, Bland-Altman analysis showed a small degree of systematic bias but large LoA regardless of model, indicating the presence of considerable variability at the sample level even in the best-performing models. This indicates that a smaller MAE does not necessarily imply a reliable prediction at the sample level.

The set of considered raw time series models also included transformer or hybrid CNN-LSTM models. PPNet, in spite of having a fairly modest parameter size ( $\sim 125k$ ), was competitive in both Calib and CalibFree cases, coming close to matching the variants of XResNet and emphasizing the potential of light-weight hybrid CNN-LSTM models. Conversely, TimesNet ( $\sim 667k$  parameters) and iTransformer ( $\sim 642k$  parameters) only modestly improved on the baseline and did not reach CNN-level accuracy. Along with the parameter study in Table 10, these indicate that model size does not directly correlate with results: AlexNet ( $>40m$  parameters) and TCNS ( $>6m$  parameters) are among the largest models and yet under-performed, yet the significantly smaller PPNet was more effective.

**Comparison to Literature Results.** The number of published results on PulseDB is very limited. To the best of our knowledge [66] is the only prior study that reported results on PulseDB, albeit on the full dataset and not just the VitalDB subset, achieving a MAE of 10-11 mmHg for SBP after self-supervised pretraining. We refer to [67] for a recent comparative analysis of different models on different datasets, where models achieved MAEs of between 11 and 19 mmHg for SBP, and between 7 and 11 mmHg for DBP. In comparison, in this study, the lowest MAEs were in the range of approximately 12–13 mmHg and 8 mmHg

for SBP and DBP, respectively, on VitalDB CalibFree. This suggests that the presented best-performing models reached state-of-the-art performance.

**Impact of Loss Function and Dropout Ensembling.** The performance of the XResNet1d50+GNLL in comparison to the XResNet1d50 trained with a regular MAE loss highlights the benefits of incorporating dropout ensembling at evaluation, and using a likelihood-based loss can have on model performance. It suggests that potentially CNN results could be improved by using a different loss function and ensemble-based evaluation procedure. Interestingly, this only applied to the Calib and not the CalibFree scenario. Other works have reported that modelling uncertainties may improve predictive performance on models trained on ECG data [68]. This variant had two parallel output branches with dropout layers (with a constant but low dropout rate, e.g. 4-5% depending on the task/parameter) dispersed throughout the architecture. Each test input was evaluated 100 times with the dropout layers left active. The predictions produced with the technique are the average of the distribution of outputs produced for each input. Also, a separate model was trained to predict each BP type (systolic/diastolic).

**Overall Performance.** The best-performing model (XResNet1d50+GNLL on Calib) achieved up to 48% of SBP estimates, and 64% of DBP estimates in the top IEEE category (Grade A), i.e. with prediction errors  $\leq 5$  mmHg. However, even with this model, 41% of SBP estimates, and 25% of DBP estimates fell into the lowest category (Grade D). For clinical applications, reducing the fraction of grade D is highly important, or at least identifying patient characteristics that allow to predict whether an unseen patient will belong to grade A or D. This task is referred to as out-of-model-scope detection [69], a task which is closely related to out-of-distribution detection. Reliable uncertainty estimation is a commonly used approach for the latter and therefore also represents a promising direction for future research. More generally, it might be insightful to assess whether coarser prediction targets, i.e. framing BP prediction as a classification target, could provide clinically meaningful insights, see [70] for an exploration.

**Limitations of the VitalDB Dataset.** VitalDB is an intraoperative vital signs dataset. Key advantages are that it includes non-cardiac patients, and it is labelled with detailed information on surgical type, surgical approach, anaesthetic type, duration, and device. The dataset covers a wide age range, from neonates to adults. For this study, it was treated as a single dataset, but further disaggregation into subgroups would be essential to identify clinically meaningful features and assess their generalizability in wider healthcare settings. Furthermore, the dataset is not representative of the key application of PPG-based BP monitoring in wearables in the general population, because data were acquired from subjects during surgery rather than in daily life, using clinical pulse oximeters rather than wearable devices. It is also worth noting that since the recordings were obtained from anesthetized patients in the controlled surgical settings, the PPG signals contain minimal motion artifacts, and hence, it might result in optimistic performance estimates when compared to real-world

wearable scenarios.

## 5.2 AF Detection

**Relative Performance Comparison.** Best performance on the classification case was achieved by modern CNN architectures (XResNet1d, Inception), which performed at least on par with, and in some cases showed advantages over, simpler models (LeNet1d). Feature-based approaches (based on wavelets) showed comparable performance to simple CNNs but were clearly outperformed by large-scale CNNs operating on raw time series input. Furthermore, it is worth noting that although PPNet’s performance was very close to the top-performing CNNs, it still fell short, whereas both iTransformer and TimesNet were distinctly inferior, highlighting the relative effectiveness of the convolutional architectures on this task. Notably, the STFT-based Spectrogram-ResNet achieved performance comparable to the top-performing raw time-series CNNs in terms of AUC, F1-score, and thresholded sensitivity and specificity, indicating that image-based representations can be competitive for AF detection. Furthermore, bootstrap analyses showed that several top-performing CNN and image-based models were statistically indistinguishable in terms of classification accuracy, suggesting that increasing architectural complexity yields diminishing returns for this data.

**Comparison to Literature Results.** The original publication describing the DeepBeat dataset [42] reported F1-scores of 0.54 for AF-prediction without pretraining and 0.71 for a multi-task model that jointly predicted AF and signal quality. It is important to stress that these results were achieved on a different, imbalanced split of the dataset and are therefore not directly comparable to those in the present study. The SiamQuality CNN model [66] achieved F1-scores of up to 0.71 on DeepBeat, albeit after self-supervised pretraining. To enable a direct comparison, we train an XResNet1d50 model on the original split and achieved an F1-score of 0.69, which is clearly superior to the model presented in the original DeepBeat publication. This demonstrates that the presented models reached state-of-the-art performance in comparison to literature benchmarks.

**Overall Performance.** The best-performing models showed a strong performance in terms of absolute performance values, with F1-scores comparable to or better than reported values in the literature (using the original splits provided by DeepBeat), and sensitivities and specificities of around 0.8. It is worth noting that even though certain commercial AF detection algorithms claim to reach 0.98 sensitivity at  $> 0.99$  specificity on internal validation datasets [71], they typically rely on ECG measurements, which serve as the gold standard for AF detection, and severely overestimate the model performance under real-world conditions as the reported performance only applies to certain heart range intervals [72]. In practice, PPG-based AF detection algorithms in consumer wearables are often designed to provide a high positive predictive value by requiring multiple predictions of AF before raising an alert [73, 74]. Further work would be required to investigate whether a high positive predictive value could be achieved on real-world data using the models presented in this study.

**CIF vs. Raw Time Series Models.** The difference in AF detection performance between raw time series models and those based on clinically interpretable features may be influenced by multiple factors, including biases in the data acquisition process, artifacts, and even errors in the labelling of recordings into different classes. Deep learning-based raw time series models can use a broad range of information from the signal, enhancing their ability to detect class-specific patterns. However, the drawback is that clinically irrelevant features, such as artifacts and biases, may be incorporated into the training process. In contrast, models that rely on predefined clinically interpretable features, such as pulse irregularity in AF, have a more constrained feature space. While this improves interpretability and robustness in some cases, it may also make these models more vulnerable to mislabelled or noisy data. Initial experiments indicate that incorporating signal quality assessments next to interpretable features can enhance prediction performance. Future work should investigate the classification performance in terms of more fine-grained subgroups, in particular stratified according to signal and labelling quality. Such analysis could reveal if feature-based methods exhibit advantages over raw time series approaches in high-quality subsets, where the underlying assumptions of clinical validity are most clearly satisfied.

**Limitations of the DeepBeat Dataset.** While the DeepBeat dataset represents one of the few publicly available PPG-based AF prediction dataset that is large enough for training deep learning models, it is very sparsely documented, and no corresponding ECG signals are available, which would allow one to retrospectively assess the annotation quality. For DeepBeat, three independent cohorts were examined: patients admitted for cardioversion before treatment (classified as AF based on patient ID rather than data window), different participants undergoing exercise stress tests and a challenge dataset as the only subset containing both AF and non-AF samples. Furthermore, the data were categorized into low-, medium-, and high-quality segments, all of which were included in this study. However, there was a notable imbalance, with a greater number of high-quality AF-labelled segments compared to non-AF-labelled segments.

Even though the DeepBeat authors demonstrated the generalization of models trained on DeepBeat to external datasets, due to the substantial differences between these datasets, we cannot conclusively attribute the observed changes solely to AF. The PPG feature variations used to classify the datasets may have resulted from other fundamental differences between them.

### 5.3 General Insights and Directions for Future Research

**General Recommendations on Model Choices.** In this study, modern CNN architectures such as XResNet1d provided the best performance in all three cases, as confirmed by both aggregate performance metrics and agreement- and bootstrap-based analyses. Therefore, our general recommendation is to use these modern CNN architectures for prediction models operating on PPG data. However, in certain cases, it may not be necessary to use such complex models

(e.g. see the Calibfree scenario of BP regression). Similarly, for certain tasks, models leveraging image representations achieved competitive results. Nevertheless, in the interest of achieving competitive results on an unknown task, the use of modern CNN architectures based on raw time series representations remains the safest choice. In spite of promising results in other applications, more complicated hybrid CNN-RNN or transformer-based models did not show any improvements over CNN-based baselines. This might not be a finding that generalizes to other datasets, but potentially just a reflection of the fact that the considered models for the respective datasets/tasks are already operating in a regime where they are largely data-constrained and already close to the optimal performance achievable on the respective datasets.

**Model Interpretability.** Beyond quantitative performance metrics, model interpretability represents a critical factor determining clinical adoption of AI systems. This interpretability challenge manifests differently across modelling approaches. Feature-based methods offer inherent interpretability advantages through clinically meaningful inputs such as pulse morphology metrics or rhythm irregularity characteristics. These inputs provide immediate physiological interpretation that clinicians can readily understand. However, when complex prediction algorithms operate on these interpretable features, the overall model often becomes opaque, negating the initial interpretability benefit.

The explainable AI (XAI) community has developed techniques to address this opacity across different input representations. Post-hoc XAI methods, applicable to already-trained models, commonly generate heatmaps that highlight input regions contributing positively or negatively to model decisions [75]. These approaches have shown promise when applied to physiological time series analysis [50]. Despite advances in XAI techniques, deep learning models operating on raw data remain fundamentally more challenging to interpret than models built on clinically meaningful features. This interpretability gap persists even with sophisticated explanation methods, creating a fundamental trade-off between model sophistication and clinical transparency.

**Robustness.** There is a second important quality dimension that is not captured explicitly by our analysis: robustness to input noise or artefacts. Note that wrist-worn PPG sensors, as used in DeepBeat, are more prone to motion artefacts and provide a lower signal-to-noise ratio relative to clinical-grade systems. But also within a single dataset, signal quality varies widely. In free-living conditions, motion artefacts often dominate wrist PPG recordings and represent one of the primary reasons why many academic PPG-based models fail to translate into reliable real-world devices. Future work should evaluate the robustness, for example, by considering predictive performance stratified according to signal quality. While datasets such as DeepBeat or MIMIC would, in principle, allow such analyses, the present study focuses on controlled, standardized evaluation settings to enable like-for-like comparison of model architectures, and therefore does not include an explicit quantitative robustness assessment. A second ro-

bustness limitation relates to the restriction of assessing the performance purely based on in-distribution performance, which is known to lead to an overly optimistic assessment of the generalization performance. This urges for dedicated studies on the out-of-distribution generalization performance of the presented models, see [76, 44] for the first studies in the context of BP prediction.

**(Self-supervised) Pretraining.** An important restriction of the presented study is the restriction to models that were trained from scratch. A very promising extension lies in the consideration of supervised or self-supervised pretraining, which, in the case of DeepBeat, leads to an increase from 0.71 to 0.91 in terms of F1-scores for the multi-task model. In particular, this applies to the recently published foundation models for PPG data [66, 77].

## 6 Summary and Conclusion

Our investigations across two exemplary regression and classification tasks found that in general modern CNNs (of the ResNet- or Inception-kind) represented the best-performing approaches. The competitiveness of small-scale models and feature-based approaches depends crucially on the definition of the task at hand. While in some scenarios (e.g. regression CalibFree), they can compete with or in some cases even outperform modern CNNs, they may fail to show competitive performance in other cases (e.g. regression Calib, classification).

### Code availability

The complete implementation, including scripts for data preprocessing as well as model training is available at <https://gitlab.com/qumphy/d1-code>.

### Generative AI statement

No generative AI was used for text generation in this manuscript.

### Competing interests

The authors have declared no competing interests.

### Ethics statement

This study used publicly available and deidentified datasets. No direct patient interaction or intervention was involved. As these datasets are released under established data use agreements and have been ethically approved for secondary research, no additional ethics approval was sought.

## Acknowledgments

The project (22HLT01 QUMPHY) has received funding from the European Partnership on Metrology, co-financed from the European Union’s Horizon Europe Research and Innovation Programme and by the Participating States. Funding for the University of Cambridge, KCL, NPL and the University of Surrey was provided by Innovate UK under the Horizon Europe Guarantee Extension, grant numbers 10091955, 10087011, 10084125, 10084961 respectively. PHC acknowledges funding from the British Heart Foundation (BHF) grant [FS/20/20/34626].

## References

- [1] P. H. Charlton, J. Allen, R. Bailón, S. Baker, J. A. Behar, F. Chen *et al.*, “The 2023 wearable photoplethysmography roadmap,” *Physiol Meas*, vol. 44, no. 11, p. 111001, 2023.
- [2] D. Castaneda, A. Esparza, M. Ghamari, C. Soltanpur, and H. Nazeran, “A review on wearable photoplethysmography sensors and their potential future applications in health care,” *Int J Biosens Bioelectron*, vol. 4, no. 4, pp. 195–202, 2018.
- [3] J. Sola, R. Vetter, P. Renevey, O. Chételat, C. Sartori, and S. F. Rimoldi, “Parametric estimation of pulse arrival time: A robust approach to pulse wave velocity,” *Physiol Meas*, vol. 30, no. 7, p. 603, 2009.
- [4] C. Ding, R. Xiao, W. Wang, E. Holdsworth, and X. Hu, “Photoplethysmography based atrial fibrillation detection: A continually growing field,” *Physiol Meas*, vol. 45, no. 4, p. 04TR01, 2024.
- [5] C. El-Hajj and P. A. Kyriacou, “Cuffless blood pressure estimation from PPG signals and its derivatives using deep learning models,” *Biomed Signal Process Control*, vol. 70, p. 102984, 2021.
- [6] G. Nie, J. Zhu, G. Tang, D. Zhang, S. Geng, Q. Zhao, and S. Hong, “A review of deep learning methods for photoplethysmography data,” *arXiv preprint arXiv:2401.12783*, 2024.
- [7] P. H. Charlton, P. Kyriacou, J. Mant, and J. Alastruey, “Acquiring wearable photoplethysmography data in daily life: The PPG diary pilot study,” *Eng Proc*, vol. 2, no. 1, p. 80, 2020.
- [8] J. C. Nielsen and Group ESD, “2024 ESC Guidelines for the management of atrial fibrillation developed in collaboration with the European Association for Cardio-Thoracic Surgery (EACTS),” *Eur Heart J*, vol. 45, no. 36, pp. 3314–414, 2024.

- [9] Group ESD, “2024 ESC Guidelines for the management of elevated blood pressure and hypertension,” *Eur Heart J*, vol. 45, no. 38, pp. 3912–4018, 2024.
- [10] O. Yildirim, U. B. Baloglu, R. S. Tan, E. J. Ciaccio, and U. R. Acharya, “A new approach for arrhythmia classification using deep coded features and LSTM networks,” *Comput Methods Programs Biomed*, vol. 176, pp. 121–33, 2019.
- [11] A. Y. Hannun, P. Rajpurkar, M. Haghpanahi, G. H. Tison, C. Bourn, M. P. Turakhia, and A. Y. Ng, “Cardiologist-level arrhythmia detection and classification in ambulatory electrocardiograms using a deep neural network,” *Nature Medicine*, vol. 25, no. 1, pp. 65–69, 2019.
- [12] R. Vanithamani, S. S. Jayabharathi, S. Pavithra, and E. S. J. Jothi, “Deep learning approaches for continuous blood pressure estimation from photoplethysmography signal,” *Measurement: Sensors*, vol. 39, p. 101866, 2025.
- [13] M. Kachuee, S. Darabi, B. Moatamed, and M. Sarrafzadeh, “Dynamic feature acquisition using denoising autoencoders,” *IEEE Trans Neural Netw Learn Syst*, vol. 30, no. 8, pp. 2252–62, 2018.
- [14] H. Mohammadi, B. Tarvirdizadeh, K. Alipour, and M. Ghamari, “Cuff-less blood pressure monitoring via PPG signals using a hybrid CNN-BiLSTM deep learning model with attention mechanism,” *Scientific Reports*, vol. 15, no. 1, p. 22229, 2025.
- [15] S. Kwon, J. Hong, E. K. Choi, E. Lee, D. E. Hostallero, W. J. Kang *et al.*, “Deep learning approaches to detect atrial fibrillation using photoplethysmographic signals: Algorithms development study,” *JMIR MHealth UHealth*, vol. 7, no. 6, p. e12770, 2019.
- [16] P. Cheng, Z. Chen, Q. Li, Q. Gong, J. Zhu, and Y. Liang, “Atrial fibrillation identification with PPG signals using a combination of time-frequency analysis and deep learning,” *IEEE Access*, vol. 8, pp. 172 692–172 706, 2020.
- [17] B. Aldughayfiq, F. Ashfaq, N. Z. Jhanjhi, and M. Humayun, “A deep learning approach for atrial fibrillation classification using multi-feature time series data from ECG and PPG,” *Diagnostics*, vol. 13, no. 14, p. 2442, 2023.
- [18] H. Ismail Fawaz, B. Lucas, G. Forestier, C. Pelletier, D. F. Schmidt, J. Weber, G. I. Webb, L. Idoumghar, P.-A. Muller, and F. Petitjean, “Inceptiontime: Finding AlexNet for time series classification,” *Data Mining and Knowledge Discovery*, vol. 34, no. 6, pp. 1936–1962, 2020.
- [19] A. Dempster, D. F. Schmidt, and G. I. Webb, “Minirocket: A very fast (almost) deterministic transform for time series classification,” in *Proceedings of the 27th ACM SIGKDD Conference on Knowledge Discovery & Data Mining*, 2021, pp. 248–57.

- [20] H. Wu, T. Hu, Y. Liu, H. Zhou, J. Wang, and M. Long, “Timesnet: Temporal 2d-variation modeling for general time series analysis,” *arXiv preprint arXiv:2210.02186*, 2022.
- [21] Y. Liu, T. Hu, H. Zhang, H. Wu, S. Wang, L. Ma, and M. Long, “itransformer: Inverted transformers are effective for time series forecasting,” *arXiv preprint arXiv:2310.06625*, 2023.
- [22] E. Eldele, M. Ragab, Z. Chen, M. Wu, and X. Li, “Tslanet: Rethinking transformers for time series representation learning,” *arXiv preprint arXiv:2404.08472*, 2024.
- [23] E. Mejia-Mejia, J. Allen, K. Budidha, C. El-Hajj, P. A. Kyriacou, and P. H. Charlton, “Photoplethysmography signal processing and synthesis,” in *Photoplethysmography*. Elsevier, 2022, pp. 69–146.
- [24] T. Pereira, N. Tran, K. Gadhoumi, M. M. Pelter, D. H. Do, R. J. Lee *et al.*, “Photoplethysmography based atrial fibrillation detection: A review,” *NPJ Digit Med*, vol. 3, no. 1, pp. 1–12, 2020.
- [25] L. M. Eerikäinen, A. G. Bonomi, L. R. Dekker, R. Vullings, and R. M. Aarts, “Atrial fibrillation monitoring with wrist-worn photoplethysmography-based wearables: State-of-the-art review,” *Cardiovasc Digit Health J*, vol. 1, no. 1, pp. 45–51, 2020.
- [26] R. Ferizoli, P. Karimpour, J. M. May, and P. A. Kyriacou, “Arterial stiffness assessment using PPG feature extraction and significance testing in an in vitro cardiovascular system,” *Sci Rep*, vol. 14, no. 1, p. 2024, 2024.
- [27] R. N. Bracewell, C. Cherry, J. F. Gibbons, W. W. Harman, H. Heffner, E. W. Herold *et al.*, *McGraw-Hill Series in Electrical and Computer Engineering*. McGraw Hill Boston, 2000.
- [28] S. Mallat, *A Wavelet Tour of Signal Processing*. Academic Press, 1999.
- [29] N. E. Huang and Z. Wu, “A review on Hilbert-Huang transform: Method and its applications to geophysical studies,” *Rev Geophys*, vol. 46, no. 2, p. 2007RG000228, 2008.
- [30] U. Hackstein, T. Krüger, A. Mair, C. Degünther, S. Krickl, C. Schlensak *et al.*, “Early diagnosis of aortic aneurysms based on the classification of transfer function parameters estimated from two photoplethysmographic signals,” *Inform Med Unlocked*, vol. 25, p. 100652, 2021.
- [31] A. Mair, M. Wisotzki, and S. Bernhard, “Classification and regression of stenosis using an in-vitro pulse wave data set: Dependence on heart rate, waveform and location,” *Comput Biol Med*, vol. 151, p. 106224, 2022.
- [32] A. Al Fahoum, A. Al Omari, G. Al Omari, and A. Zyout, “PPG signal-based classification of blood pressure stages using wavelet transformation and pre-trained deep learning models,” in *2023 Computing in Cardiology Conference (CinC)*, 2023, pp. 1–4.

- [33] J. Wu, H. Liang, C. Ding, X. Huang, J. Huang, and Q. Peng, “Improving the accuracy in classification of blood pressure from photoplethysmography using continuous wavelet transform and deep learning,” *Int J Hyperten*, vol. 2021, no. 1, p. 9938584, 2021.
- [34] A. Neshitov, K. Tyapochkin, E. Smorodnikova, and P. Pravdin, “Wavelet analysis and self-similarity of photoplethysmography signals for HRV estimation and quality assessment,” *Sensors*, vol. 21, no. 20, p. 6798, 2021.
- [35] J. Chen, K. Sun, Y. Sun, and X. Li, “Signal quality assessment of PPG signals using STFT time-frequency spectra and deep learning approaches,” in *Proceedings of the 43rd Annual International Conference of the IEEE Engineering in Medicine & Biology Society (EMBC)*. IEEE, 2021, pp. 1153–1156.
- [36] V. S. Roha, R. Ranjan, and M. R. Yuce, “Evolving blood pressure estimation: From feature analysis to image-based deep learning models,” *Journal of Medical Systems*, vol. 49, no. 1, p. 97, 2025.
- [37] Z. Wang and T. Oates, “Imaging time-series to improve classification and imputation,” *arXiv preprint arXiv:1506.00327*, 2015.
- [38] W. Wang, P. Mohseni, K. L. Kilgore, and L. Najafizadeh, “Cuff-less blood pressure estimation from photoplethysmography via visibility graph and transfer learning,” *IEEE Journal of Biomedical and Health Informatics*, vol. 26, no. 5, pp. 2075–2085, 2021.
- [39] P. J. Aston, M. I. Christie, Y. H. Huang, and M. Nandi, “Beyond HRV: Attractor reconstruction using the entire cardiovascular waveform data for novel feature extraction,” *Physiol Meas*, vol. 39, p. 024001, 2018.
- [40] J. V. Lyle and P. J. Aston, “Symmetric Projection Attractor Reconstruction: Embedding in higher dimensions,” *Chaos*, vol. 31, p. 113135, 2021.
- [41] W. Wang, P. Mohseni, K. L. Kilgore, and L. Najafizadeh, “PulseDB: A large, cleaned dataset based on MIMIC-III and VitalDB for benchmarking cuff-less blood pressure estimation methods,” *Front Digit Health*, vol. 4, p. 1090854, 2023.
- [42] J. Torres-Soto and E. A. Ashley, “Multi-task deep learning for cardiac rhythm detection in wearable devices,” *NPJ Digit Med*, vol. 3, no. 1, p. 116, 2020.
- [43] H. C. Lee, Y. Park, S. B. Yoon, S. M. Yang, D. Park, and C. W. Jung, “VitalDB, a high-fidelity multi-parameter vital signs database in surgical patients,” *Sci Data*, vol. 9, no. 1, p. 279, 2022.
- [44] M. Moulaeifard, P. H. Charlton, and N. Strodthoff, “Generalizable deep learning for photoplethysmography-based blood pressure estimation – a benchmarking study,” *Machine Learning: Health*, Sep. 2025. [Online]. Available: <http://dx.doi.org/10.1088/3049-477X/ae01a8>

- [45] S. Joung, J. Kim, J. Park *et al.*, “Continuous cuffless blood pressure monitoring using photoplethysmography-based PPG2BP-net for high intrasubject blood pressure variations,” *IEEE J Biomed Health Inform*, 2021.
- [46] J. M. Bland and D. G. Altman, “Statistical methods for assessing agreement between two methods of clinical measurement,” *The Lancet*, vol. 327, no. 8476, pp. 307–310, 1986.
- [47] *IEEE Standard for Wearable, Cuffless Blood Pressure Measuring Devices – Amendment 1*, Institute of Electrical and Electronics Engineers (IEEE) Std. IEEE Std 1708a-2019 Amend IEEE Std 1708-2014, 2019. [Online]. Available: <https://ieeexplore.ieee.org/document/8859683>
- [48] G. S. Stergiou, R. Giovannini, G. Mancina, P. W. de Leeuw, Y. Imai, J. Wang, G. Parati, R. Asmar, and E. O’Brien, “A universal standard for the validation of blood pressure measuring devices: Association for the Advancement of Medical Instrumentation/European Society of Hypertension/International Organization for Standardization (AAMI/ESH/ISO) Collaboration Statement,” *Hypertension*, vol. 71, no. 3, pp. e102–e107, 2018.
- [49] E. O’Brien, J. C. Petrie, W. A. Littler, P. L. Padfield, K. O’Malley, and M. Jamieson, “The British Hypertension Society protocol for the evaluation of blood pressure measuring devices,” *J Hyperten*, vol. 11, no. Suppl 2, pp. S43–S62, 1993.
- [50] P. Wagner, T. Mehari, W. Haverkamp, and N. Strodthoff, “Explaining deep learning for ECG analysis: Building blocks for auditing and knowledge discovery,” *Comp Biol Med*, vol. 176, p. 108525, 2024.
- [51] N. Strodthoff, P. Wagner, T. Schaeffter, and W. Samek, “Deep learning for ECG analysis: Benchmarks and insights from PTB-XL,” *IEEE J Biomed Health Inform*, vol. 25, no. 5, pp. 1519–28, 2020.
- [52] B. Lakshminarayanan, A. Pritzel, and C. Blundell, “Simple and scalable predictive uncertainty estimation using deep ensembles,” *Adv Neural Inf Process Syst*, vol. 30, 2017.
- [53] A. Krizhevsky, I. Sutskever, and G. E. Hinton, “Imagenet classification with deep convolutional neural networks,” *Adv Neural Inf Process Syst*, vol. 25, 2012.
- [54] S. Bai, J. Z. Kolter, and V. Koltun, “An empirical evaluation of generic convolutional and recurrent networks for sequence modeling,” *arXiv preprint 1803.01271*, 2018.
- [55] M. Panwar, A. Gautam, D. Biswas, and A. Acharyya, “PP-Net: A deep learning framework for ppg-based blood pressure and heart rate estimation,” *IEEE Sensors Journal*, vol. 20, no. 17, pp. 10 000–10 011, 2020.

- [56] P. H. Charlton, P. Celka, B. Farukh, P. Chowienczyk, and J. Alastruey, “Assessing mental stress from the photoplethysmogram: A numerical study,” *Physiol Meas*, vol. 39, no. 5, p. 054001, 2018.
- [57] S. Dash, K. H. Chon, S. Lu, and E. A. Raeder, “Automatic real time detection of atrial fibrillation,” *Ann Biomed Eng*, vol. 37, no. 9, pp. 1701–9, 2009.
- [58] K. Tateno and L. Glass, “Automatic detection of atrial fibrillation using the coefficient of variation and density histograms of RR and  $\Delta$ RR intervals,” *Med. Biol. Eng. Comput.*, vol. 39, no. 6, pp. 664–671, 2001.
- [59] P. Langley, M. Dewhurst, L. Y. Di Marco, P. Adams, F. Dewhurst, J. C. Mwita *et al.*, “Accuracy of algorithms for detection of atrial fibrillation from short duration beat interval recordings,” *Med Eng Phys*, vol. 34, no. 10, pp. 1441–7, 2012.
- [60] A. Petrėnas, V. Marozas, and L. Sörnmo, *Atrial Fibrillation from an Engineering Perspective*. Springer, 2018.
- [61] C. E. Rasmussen, “Gaussian Processes in machine learning,” in *Advanced Lectures on Machine Learning: ML Summer Schools 2003*, O. Bousquet, U. von Luxburg, and G. Rätsch, Eds. Springer, 2004, pp. 63–71.
- [62] H. M. Rai, A. Trivedi, and S. Shukla, “ECG signal processing for abnormalities detection using multi-resolution wavelet transform and artificial neural network classifier,” *Measurement*, vol. 46, no. 9, pp. 3238–46, 2013.
- [63] K. He, X. Zhang, S. Ren, and J. Sun, “Deep residual learning for image recognition,” in *Proceedings of the IEEE Conference on Computer Vision and Pattern Recognition (CVPR)*, 2016, pp. 770–778.
- [64] J. Deng, W. Dong, R. Socher, L.-J. Li, K. Li, and L. Fei-Fei, “Imagenet: A large-scale hierarchical image database,” in *Proceedings of the IEEE Conference on Computer Vision and Pattern Recognition (CVPR)*, 2009.
- [65] K. He, X. Zhang, S. Ren, and J. Sun, “Deep residual learning for image recognition,” in *Proceedings of the IEEE Conference on Computer Vision and Pattern Recognition (CVPR)*, 2016.
- [66] C. Ding, Z. Guo, Z. Chen, R. J. Lee, C. Rudin, and X. Hu, “SiamQuality: A ConvNet-based foundation model for photoplethysmography signals,” *Physiol Meas*, vol. 45, no. 8, p. 085004, 2024.
- [67] S. González, W. T. Hsieh, and T. P. C. Chen, “A benchmark for machine-learning based non-invasive blood pressure estimation using photoplethysmogram,” *Sci Data*, vol. 10, no. 1, p. 149, 2023.
- [68] J. F. Vranken, R. R. van de Leur, D. K. Gupta, L. E. Juarez Orozco, R. J. Hassink, P. van der Harst *et al.*, “Uncertainty estimation for deep learning-based automated analysis of 12-lead electrocardiograms,” *Eur Heart J-Digit Health*, vol. 2, no. 3, pp. 401–15, 2021.

- [69] J. Guérin, K. Delmas, R. Ferreira, and J. Guiochet, “Out-of-distribution detection is not all you need,” in *Proceedings of the AAAI Conference on Artificial Intelligence*, 2023, pp. 14 829–37.
- [70] F. Schrumpf, P. R. Serdack, and M. Fuchs, “Regression or classification? reflection on bp prediction from ppg data using deep neural networks in the scope of practical applications,” in *Proceedings of the IEEE/CVF Conference on Computer Vision and Pattern Recognition*, 2022, pp. 2172–81.
- [71] D. R. Seshadri, B. Bittel, D. Browsky, P. Houghtaling, C. K. Drummond, M. Y. Desai *et al.*, “Accuracy of apple watch for detection of atrial fibrillation,” *Circulation*, vol. 141, no. 8, pp. 702–3, 2020.
- [72] W. Haverkamp, J. Butler, and S. D. Anker, “Can we trust a smartwatch ECG? Potential and limitations,” *Eur J Heart Fail*, vol. 23, no. 6, pp. 850–3, 2021.
- [73] S. A. Lubitz, A. Z. Faranesh, C. Selvaggi, S. J. Atlas, D. D. McManus, D. E. Singer *et al.*, “Detection of atrial fibrillation in a large population using wearable devices: The fitbit heart study,” *Circulation*, vol. 146, no. 19, pp. 1415–24, 2022.
- [74] M. V. Perez, K. W. Mahaffey, H. Hedlin, J. S. Rumsfeld, A. Garcia, T. Ferris *et al.*, “Large-scale assessment of a smartwatch to identify atrial fibrillation,” *N Engl J Med*, vol. 381, no. 20, pp. 1909–17, 2019.
- [75] A. Holzinger, A. Saranti, C. Molnar, P. Biecek, and W. Samek, “Explainable AI methods - a brief overview,” in *International Workshop on Extending Explainable AI Beyond Deep Models and Classifiers*. Springer, 2020, pp. 13–38.
- [76] G. Weber-Boisvert, B. Gosselin, and F. Sandberg, “Intensive care photoplethysmogram datasets and machine-learning for blood pressure estimation: Generalization not guaranteed,” *Front Physiol*, vol. 14, Mar. 2023.
- [77] A. Pillai, D. Spathis, F. Kawsar, and M. Malekzadeh, “PaPaGei: Open foundation models for optical physiological signals,” *arXiv preprint 2410.20542*, 2025.

## A Supplementary material

### A.1 Background

#### A.1.1 BP estimation

BP is one of the most widely used physiological measurements. It is a key marker of cardiovascular health; a valuable predictor of cardiovascular events; and is essential for the selection and monitoring of antihypertensive (BP lowering) treatments. However, there are several limitations to BP measurements currently taken in a clinical setting. First, clinical BP measurements are not taken frequently in the wider population, meaning many people around the world are not aware that they have high blood pressure. Second, clinical BPs can be unrepresentative of a patient’s normal BP due to the white coat hypertension effect, where a patient’s BP is higher in the clinical setting than normal life. Third, they provide only a snapshot of blood pressure at a single time point, and do not capture diurnal variations which contain important information on health. Fourth, cuff-based blood pressure devices are not suitable for long-term monitoring. Consequently, it would be highly valuable to develop technology to monitor fluctuations in BP, unobtrusively in daily life, such as in wearables.

PPG-based BP estimation provides a potential approach to monitor BP unobtrusively in daily life. PPG is now widely incorporated into consumer wearable devices, and PPG signals vary with BP. Researchers have focused on two main approaches to estimating BP from PPG signals <sup>1</sup>: (i) using the shape of a single PPG pulse wave; and (ii) using the speed at which the pulse wave propagates through the arteries (the pulse wave velocity). In this project, we focus on the first approach, since it can be implemented in many common wearables such as smartwatches, whereas the second requires simultaneous measurements at different anatomical sites. BP can potentially be estimated from the shape of the pulse wave using traditional signal processing based on expert-identified features, or using deep learning techniques which learn how the pulse wave is affected by BP changes for themselves.

#### A.1.2 AF detection

AF is the most common sustained cardiac arrhythmia and confers a five-fold increase in stroke risk. Fortunately, the risk of stroke can be greatly reduced via anticoagulation. However, patients with AF are often underdiagnosed, either because AF episodes occur asymptotically or because it occurs only intermittently and so is not identified during routine testing. Therefore, there is a need for continuous unobtrusive heart rhythm monitoring to identify patients with AF.

---

<sup>1</sup>Charlton PH *et al.*, ‘Assessing hemodynamics from the photoplethysmogram to gain insights into vascular age: a review from VascAgeNet’, *American Journal of Physiology-Heart and Circulatory Physiology*, 322(4), H493–H522, 2022. <https://doi.org/10.1152/ajpheart.00392.2021>

PPG provides an attractive approach to identifying AF because it is widely used in consumer wearables, and because it provides a measure of the heart rhythm, which is irregular during AF. Indeed, several smartwatches used PPG to identify irregular rhythms which may be indicative of AF<sup>2</sup>. Irregular heart rhythms have been identified from PPG signals by identifying individual pulse waves corresponding to heartbeats, extracting inter-beat intervals, and assessing the level of inter-beat interval variability, where higher levels of variability indicate higher levels of irregularity. More recently, deep learning models have been developed to identify AF from the PPG signal<sup>3</sup>.

## A.2 Original DeepBeat dataset

This dataset includes over 500,000 signal segments, each with a duration of 25 seconds and a sampling rate of 32 Hz, from 175 individuals, including 108 with AF and 67 without AF (Table 9). The small test set and the overlapping signal segments of the original dataset affected the analysis. This redundancy led to inflated performance metrics, while the unbalanced distribution of AF and non-AF subjects across training, validation and test sets further biased the results. Consequently, despite its impressive performance on the test set, the original model showed reduced effectiveness on validation and training data. Finally, it is important to note key limitations of this dataset for our study, all signal segments classified as AF were collected from one study protocol where patients came in for a clinical procedure. In contrast, all signal segments classified as non-AF were collected from an independent study where subjects were doing an exercise stress test. Therefore, different devices, human subject parameters (comorbidities, heart rate) would have likely influenced the classification performance, independently of AF. Therefore, confirmatory studies on independent datasets are required before any conclusions about AF classification can be drawn.

Set	Subjects	Total samples	AF samples	Non-AF samples	Data ratio	AF ratio
Train	137	2799784	1269660	1540124	0.839	0.45
Validation	16	518782	47706	471175	0.156	0.09
Test	22	17617	4230	13387	0.005	0.24

Table 9: Original DeepBeat (Stanford Wearable PPG) Dataset

<sup>2</sup>Perez, M. V. *et al.* (2019). Large-scale assessment of a smartwatch to identify atrial fibrillation. *New England Journal of Medicine*, 381(20), 1909–1917. <https://doi.org/10.1056/NEJMoa1901183>

<sup>3</sup>Ding, C. *et al.* (2024). PPG-based AF detection: A continually growing field. *Physiological Measurement*, 45(4), 04TR01. <https://doi.org/10.1088/1361-6579/ad37ee>

### A.3 Performance evaluation and metrics

**BP regression** In our BP regression task, we use the  $L_1$  norm to evaluate and compare the performance of the machine learning models. Specifically, we employ the empirical equivalent of this norm, known as the *Mean Absolute Error* (MAE), defined as follows:

$$MAE = \frac{1}{N} \sum_{i=1}^N |y_i - \widehat{y}_i|, \quad (1)$$

where  $y_i$  denotes the ground truth values, and  $\widehat{y}_i$  the predictions made by the machine learning model on the test set.

**AF classification** Detection performance is evaluated by counting the correctly detected AF cases (true positives,  $N_{TP}$ ), correctly detected non-AF cases (true negatives,  $N_{TN}$ ), falsely detected AF cases (false positives,  $N_{FP}$ ), and missed AF cases (false negatives,  $N_{FN}$ ). Here, the term "case" refers to a segment. Using these four counts, several commonly used performance metrics are calculated.

*Sensitivity* (Se) describes the probability of a positive result given that the sample is truly positive, i.e.

$$Se = \frac{N_{TP}}{N_{TP} + N_{FN}}. \quad (2)$$

*Specificity* (Sp) describes the probability of a negative result given that the sample is truly negative, i.e.

$$Sp = \frac{N_{TN}}{N_{TN} + N_{FP}}. \quad (3)$$

The *receiver operating characteristic* (ROC) curve illustrates the performance of a binary classifier at varying threshold values by depicting the rate of truly classified positives against the rate of falsely classified positives. The area *under the curve* (AUC) of the ROC indicates the overall model performance by integrating the ROC over the threshold. The AUC ranges from 0 to 1, with 1 representing perfect detection of positives and negatives and 0 representing perfect misclassification. Moreover, a value of 0.5 represents random classification of the samples. We note that although AUC is widely used, it integrates sensitivity and specificity across both relevant and irrelevant clinical regions and is sensitive to dataset imbalance<sup>4,5</sup>. Therefore, it is most useful to understand

<sup>4</sup>Lobo, J. M., Jiménez-Valverde, A., & Real, R. (2008). AUC: a misleading measure of the performance of predictive distribution models. *Global Ecology and Biogeography*, 17(2), 145-151.

<sup>5</sup>Hanczar, B., Hua, J., Sima, C., Weinstein, J., Bittner, M., & Dougherty, E. R. (2010). Small-sample precision of ROC-related estimates. *Bioinformatics*, 26(6), 822-830.

model performance under different parameter settings during training rather than report general model performance<sup>6</sup>.

The F1 score describes the harmonic mean of the *precision*, i.e., the rate of true positives against the number of all positive labels, and the *recall*, i.e., the rate of true positives against the number of all truly positive samples and describes the overall performance of a classifier. The F1 score is defined via

$$F_1 = \frac{2 N_{TP}}{2 N_{TP} + N_{FP} + N_{FN}}. \quad (4)$$

The F1 score ranges from 0 to 1, with 1 indicating perfect detection and 0.5 indicating performance equivalent to random detection.

The Matthew’s correlation coefficient (MCC) measures the difference between the predicted values of a classifier and the actual class values. MCC is equivalent to the  $\chi^2$ -statistics for a 2 x 2 contingency table. The MCC is defined via

$$MCC = \frac{N_{TP}N_{TN} - N_{FP}N_{FN}}{\sqrt{(N_{TP} + N_{FP})(N_{TP} + N_{FN})(N_{TN} + N_{FP})(N_{TN} + N_{FN})}}. \quad (5)$$

In the original form, MCC ranges from -1 to 1, where 1 indicates perfect detection and -1 indicates complete inverse detection. For easier comparison, MCC is typically normalized<sup>7</sup>, however, note that MCC, in contrast to the F1 score, accounts for the number of correctly classified true negatives. MCC is especially useful for imbalanced datasets, as it reflects performance when most AF and non-AF episodes are accurately detected.

In binary classification, the model outputs a raw class confidence value between 0 and 1. However, most evaluation metrics require a binary classified value as input. To classify a sample using the confidence value, we set a classification threshold. If the confidence is below this threshold, the sample is assigned to the negative class; otherwise, it is assigned to the positive class. The threshold is an arbitrary parameter that can be set to achieve the best performance.

For the F1 score, we set the threshold to the naive value of 0.5. The AUC score uses the raw confidence value and does not require a threshold. For the remaining metrics, we choose the threshold that achieves a sensitivity (specificity) on the test set that is closest to, but greater than, 0.8. Once this threshold is set, we calculate the remaining metrics and denote them accordingly.

<sup>6</sup>Butkuvienė, M., Petrėnas, A., Sološenko, A., Martín-Yebra, A., Marozas, V., & Sörnmo, L. (2021). Considerations on performance evaluation of atrial fibrillation detectors. *IEEE Transactions on Biomedical Engineering*, 68(11), 3250-3260.

<sup>7</sup>Chicco, D., & Jurman, G. (2020). The advantages of the Matthews correlation coefficient (MCC) over F1 score and accuracy in binary classification evaluation. *BMC genomics*, 21, 1-13.

## A.4 Methods

### A.4.1 Raw Time Series Models

Researchers have investigated a variety of deep learning models for the prediction of BP using PPG and electrocardiogram (ECG) signals. For instance, a study by Kachuee et al. (2017)<sup>8</sup> developed a deep neural network model to estimate BP using ECG and PPG signals, which showed significant improvements in accuracy and reliability compared to traditional methods.

Another notable study by Liang et al. (2018)<sup>9</sup> introduced a hybrid model that integrates CNN and recurrent RNN to exploit both spatial and temporal features of PPG and ECG signals. This model exhibited enhanced performance in continuous blood pressure monitoring, highlighting the potential of deep learning in medical signal processing. It is worth mentioning that transfer learning has been applied to improve the performance of BP prediction models. Zhang et al. (2020)<sup>10</sup> utilized a pre-trained deep learning model and fine-tuned it with a smaller dataset of PPG and ECG signals. This approach minimized the requirement for extensive labelled data, enhancing the practicality of the model for real-world applications.

In this project, we employ prominent models such as LeNet1d<sup>11</sup>, Inception1d<sup>12</sup>, XResNet50d, XResNet101d<sup>13</sup>, AlexNet1d<sup>14</sup> and Minirocket<sup>15</sup> as well as Temporal Convolutional Networks, to conduct a thorough assessment of the outcomes.

**Baseline** The baseline model predicts BP by using the median value of the BP data, providing a straightforward reference for evaluating the performance of more advanced predictive models.

---

<sup>8</sup>Kachuee, M., Kiani, M. M., Mohammadzade, H., & Shabany, M. (2017). Cuffless BP estimation algorithms for continuous health-care monitoring. *IEEE Transactions on Biomedical Engineering*, 64(4), 859-869.

<sup>9</sup>Liang, Y., Chen, Z., Ward, R., & Elgendi, M. (2018). Hypertension assessment via ECG and PPG signals: An evaluation using machine learning models. *Computational and Mathematical Methods in Medicine*, 2018, Article 3179780

<sup>10</sup>Zhang, Y., Feng, X., Li, J., Li, B., & Peng, X. (2020). Transfer learning for hybrid deep neural network-based BP estimation. *Journal of Healthcare Engineering*, 2020, Article 5462540.

<sup>11</sup>LeCun, Y., Bottou, L., Bengio, Y., & Haffner, P. (1998). Gradient-based learning applied to document recognition. *Proceedings of the IEEE*, 86(11), 2278-2324.

<sup>12</sup>Szegedy, C., Liu, W., Jia, Y., Sermanet, P., Reed, S., Anguelov, D., ... & Rabinovich, A. (2015). Going deeper with convolutions. In *Proceedings of the IEEE conference on computer vision and pattern recognition* (pp. 1-9).

<sup>13</sup>Strodthoff, Nils, Temesgen Mehari, Claudia Nagel, Philip J. Aston, Ashish Sundar, Claus Graff, Jørgen K. Kanters et al. "PTB-XL+, a comprehensive electrocardiographic feature dataset." *Scientific data* 10, no. 1 (2023): 279.

<sup>14</sup>Krizhevsky, Alex, Ilya Sutskever, and Geoffrey E. Hinton. "Imagenet classification with deep convolutional neural networks." *Advances in neural information processing systems* 25 (2012).

<sup>15</sup>Dempster, Angus, Daniel F. Schmidt, and Geoffrey I. Webb. "Minirocket: A very fast (almost) deterministic transform for time series classification." *Proceedings of the 27th ACM SIGKDD conference on knowledge discovery & data mining*. 2021.

**XResNetd50 /101** XResNet50d and XResNet101d represent deep learning state-of-the-art models derived from ResNet architecture. They incorporate more layers, 50 and 101 layers, respectively, with a number of other enhancements, including group normalization and the option for selective kernel sizes. This allows these models to learn even more intricate hierarchical features and to be very powerful in tasks dealing with complex time-series data. The GNLL variant featured two parallel output branches and dropout layers dispersed throughout the architecture. Separate models were trained for SBP and DBP prediction for each dataset. Each input was evaluated 100 times with dropout layers left active, and the prediction is the mean of the output means.

**Inception1d** Inspired by the Inception architecture but for one-dimensional signals, it uses parallel convolutional layers with different kernel sizes. This model captures information at multiple scales, enabling the model to understand complex patterns in time series better.

**LeNet1d** LeNet1 is a one-dimensional convolutional neural network adapted from the original LeNet architecture, which is optimized for time-series data analysis. Considering a greater number of convolutional and pooling layers, it is more appropriate for extracting features from univariate signals, such as PPG or ECG.

**AlexNet1d** The AlexNet1d is a 1-dimensional adaptation of the popular convolutional neural network (CNN) architecture, traditionally used for 2D image classification. This model consists of two primary components:

1. Feature Extractor: A stacked series of convolutional, ReLU (Rectified Linear Unit), and max pooling layers.
2. Classifier: A fully connected neural network comprising two linear layers, each followed by a ReLU activation function and a dropout layer, to prevent overfitting. The final layer is a linear layer that outputs the model's predictions.

During training, we use the Gaussian negative log likelihood as the cost function, allowing the model to learn the mean and standard deviation of the predictive probability density.

**MiniRocket** The MiniRocket is an almost deterministic transform for time-series data, followed by a linear classifier. This approach uses dilated convolutions with kernels of length 9 and all possible permutations of the weights -1 and 2 that sum up to 0, where the dilation values are selected to be within a fixed range relative to the input length. Following the convolution, features are extracted by calculating the proportion of positive values in each convolution output, which is the number of positive values, divided by the sequence length.

This process yields a total of 9,996 features, which are then fed into a linear regressor to predict, in our case, the mean and standard deviation of a Gaussian predictive probability density.

The kernels do not require training, allowing for a one-time feature extraction. This enables efficient model training, as only the linear regressor needs to be trained over multiple epochs. This makes the MiniRocket a very fast and effective baseline for time-series classification and regression tasks.

**PPNet** The PPNet incorporates CNNs and LSTMs units to deal with physiological time series. CNNs characterize local spatial patterns in biosignals, and LSTMs are responsible for handling temporal dependencies, ultimately creating an efficient model to differentiate complex biomedical patterns.

**iTransformer** iTransformer turns the classical transformer on its head by applying self-attention across features instead of time steps. Each variable is treated as a token, and the model can look at inter-variable interactions. Instance-normalization specificity also preserves signal characteristics, and there are improved results on multivariate time-series forecasting tasks.

**TimesNet** TimesNet adopts an inception-style convolution architecture specific to time series. Through parallel convolutions with different receptive fields, it characterizes multi-periodic patterns in different scales in time.

**Temporal Convolutional Networks (TCNs)** Temporal Convolutional Networks (TCNs) are a class of neural networks designed for sequential data processing. Their ability to capture both short-term and long-term dependencies makes them particularly effective for analyzing complex biological time series signals, such as electrocardiograms (ECGs), electroencephalograms (EEGs), and other physiological measurements. TCNs have been used for both forecasting and classification tasks<sup>16,17,18</sup> yet, to the best of our knowledge, TCNs have never been used for the analysis of PPG signals while we believe TCNs can be relevant for such a task. Indeed, TCNs leverage the strengths of convolutional neural networks (CNNs) and adapt them for temporal data. Unlike recurrent neural networks (RNNs) that process data sequentially, TCNs use convolutional layers to capture temporal dependencies, allowing for parallel processing and typically achieving faster training times. TCNs main features are:

---

<sup>16</sup>Lin, Y., Koprinska, I., & Rana, M. (2020). Temporal Convolutional Neural Networks for Solar Power Forecasting, 2020 International Joint Conference on Neural Networks (IJCNN), Glasgow, UK, 2020, pp. 1-8, doi: 10.1109/IJCNN48605.2020.9206991.

<sup>17</sup>Pelletier, C., Webb, G. I., & Petitjean, F. (2019). Temporal convolutional neural network for the classification of satellite image time series. *Remote Sensing*, 11(5), 523.

<sup>18</sup>Hewage, P., Behera, A., Trovati, M., Pereira, E., Ghahremani, M., Palmieri, F., & Liu, Y. (2020). Temporal convolutional neural (TCN) network for an effective weather forecasting using time-series data from the local weather station. *Soft Computing*, 24, 16453-16482.

- **Causal Convolutions:** They ensure that predictions at time  $t$  are only influenced by inputs from time  $t$  and earlier to maintain the temporal order.

$$y(t) = \sum_{i=0}^{k-1} w_i x(t-i)$$

where  $x(t)$  and  $y(t)$  are respectively the input and output at time  $t$ ,  $w_i$  are the weights of the convolution filter, and  $k$  stands for the filter size. This equation ensures that the output  $y(t)$  depends only on the current and previous inputs, preserving the causality.

- **Dilated Convolutions:** They allow to capture long-range dependencies using a large receptive field without increasing computational load.

$$y(t) = \sum_{i=0}^{k-1} w_i x(t-d \cdot i)$$

where  $d$  represents the dilation factor (which determines the spacing between the elements of the input signal). Dilated convolutions allow the network to cover a larger range of inputs without increasing the number of parameters. Indeed, a dilated convolution lets the network look back up to  $dk$  time steps, enabling exponentially larger receptive fields per the number of layers. In the original paper, the authors increased  $d$  exponentially with the depth of the network.

- **Residual Connections:** They help to mitigate the vanishing gradient problem and improve the training of deeper networks.

#### A.4.2 Clinically Interpretable Feature (CIF)-Based Models

**Preprocessing** Raw PPG signals often show reduced quality due to motion artifacts, baseline drift, and hypoperfusion. Motion artifacts result from body movement or improper sensor attachment, introducing signal fluctuations that degrade signal quality. Baseline drift, caused by respiration and body movements, shifts the PPG waveform and may obscure the true pulsatile component. Hypoperfusion, characterized by reduced peripheral blood flow due to vasoconstriction, weakens PPG signals, affecting the accuracy and reliability of physiological measurements.

While CNN-based deep learning networks develop custom filter banks during training and require no specific preprocessing, expert-crafted feature-based methods necessitate signal preparation. Typically, the lower bound of the pass-band ( $\sim 0.5$  Hz) removes components below 0.1 Hz and respiratory influences in the 0.1–0.5 Hz range, preserving the AC component. The upper bound ( $\sim 5$ –10 Hz) retains primary PPG frequency components, often captured using Butterworth, Chebyshev II, or finite impulse response (FIR) filters.

In this study, for BP estimation, PPG segments from the VitalDB dataset were preprocessed using a Butterworth infinite impulse response zero-phase band-pass filter (4th order, 0.4-7 Hz). For atrial fibrillation detection, PPG segments from the DeepBeat dataset were preprocessed using low-pass, high-pass, and adaptive filters. High-frequency noise and artifacts were removed using a low-pass infinite impulse response filter (cutoff 6 Hz), while baseline wander was eliminated using a high-pass infinite impulse response filter (cutoff 0.5 Hz) and a fifth-order normalized least mean squares adaptive filter with a reference input of unity.

### Feature extraction for BP estimation

**Clinically Interpretable Features** To estimate BP, 28 PPG features<sup>19</sup> were assessed based on pulse morphology analysis and pulse derivative features (Figure 2), which are features selected from the literature<sup>24</sup> as the most significant for BP estimation.

PPG pulse wave features include amplitude-related parameters such as the amplitudes of the first ( $P_1$ ), second ( $P_2$ ) and third ( $P_3$ ) pulse waveforms<sup>20</sup>, and derived indices like the  $P_2/P_1$  ratio, reflection index ( $RI = P_3/P_1$ ), and augmentation index ( $AI = (P_1 - P_3)/P_1$ ). Time-related features consist of the pulse duration ( $T_p$ ), diastolic duration ( $T_d$ ), systolic duration ( $T_1$ ), and the time interval from  $P_1$  to  $P_3$  ( $\Delta t$ ). Area-related features include the systolic area ( $A_1$ ), diastolic area ( $A_2$ ), the inflection point area ratio ( $IPA = A_2/A_1$ ), and the inflection point area plus the d-wave amplitude of the second PPG derivative ( $IPAD$ ).

PPG derivative features include amplitude-related parameters such as ratios of the second PPG derivative waveform amplitudes ( $b/a$ ,  $c/a$ ,  $d/a$ , and  $e/a$ ), the cardiovascular aging index ( $AGI = (b-c-d-e)/a$ ) for arterial stiffness assessment, the interval aging index ( $AGI_{int} = (b-e)/a$ ), and the modified aging index ( $AGI_{mod} = (b-c-d)/a$ ). Time-related features include time intervals between second PPG derivative waves ( $t_{b-a}$ ,  $t_{b-c}$ ,  $t_{b-d}$ ). Slope-related features include the slope coefficients ( $slope_{b-c}$ ,  $slope_{b-d}$ ) of straight lines between amplitudes of  $b$  and  $c$ , and  $b$  and  $d$  waves, respectively.

**(Quasi)-periodic signal features** To solve the BP regression problem, we employ a Wavelet Packet Decomposition (WPD) approach using the Discrete Wavelet Transform (DWT) for feature extraction from raw PPG-signals. Specifically, we utilize the Daubechies wavelet (db6) of order 3, which offers a balance

<sup>19</sup>Charlton, P. H., Celka, P., Farukh, B., Chowienczyk, P., & Alastruey, J. (2018). Assessing mental stress from the photoplethysmogram: a numerical study. *Physiological measurement*, 39(5), 054001.

<sup>20</sup>Kontaxis, S., Gil, E., Marozas, V. et al. (2021) Photoplethysmographic waveform analysis for autonomic reactivity assessment in depression. *IEEE Trans. Biomed. Engng.* 68(4), 1273–1281

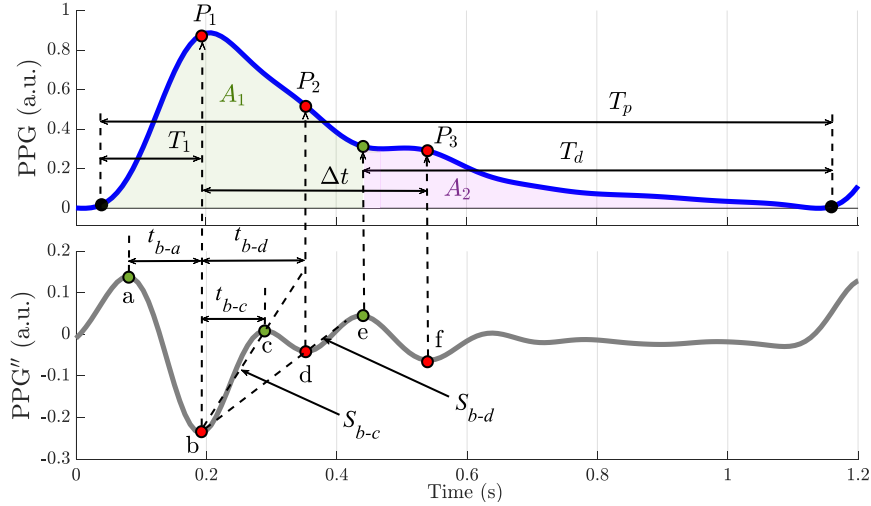


Figure 2: The definition of PPG pulse wave morphology features. Higher-order statistical features extracted from PPG pulse waveforms include skewness and kurtosis, with the latter being the most statistically significant feature for blood pressure estimation.

between time and frequency localization, making it particularly suitable for analysing non-stationary signals.

The wavelet packet decomposition allows for a hierarchical representation of the signal by decomposing both the approximation and detail the coefficients at each level. This provides a finer level of signal analysis compared to standard DWT, capturing more detailed information across different frequency bands.

After obtaining the wavelet packet coefficients, these features are flattened and then directly fed, without additional processing, as inputs to an MLP model. This simple approach will also be used to diagnose AF from PPG-signals.

### Feature extraction for AF detection

**Irregularity features** The irregularities in peak-to-peak (PP) intervals extracted from PPG signals can be evaluated based on measures of randomness, variability, and complexity<sup>21</sup>. The structure of an MLP-based atrial fibrillation detection algorithm using clinically interpretable features extracted from the PPG signal is shown in Figure 3.

Figure 4 to Figure 7 show PP intervals extracted from 25-s duration PPG segments which are of good quality with AF, good quality without AF, bad quality

<sup>21</sup>Petrėnas, A., & Marozas, V. (2018). Atrial fibrillation from an engineering perspective (pp. 137-220). L. Sörnmo (Ed.). Berlin: Springer.

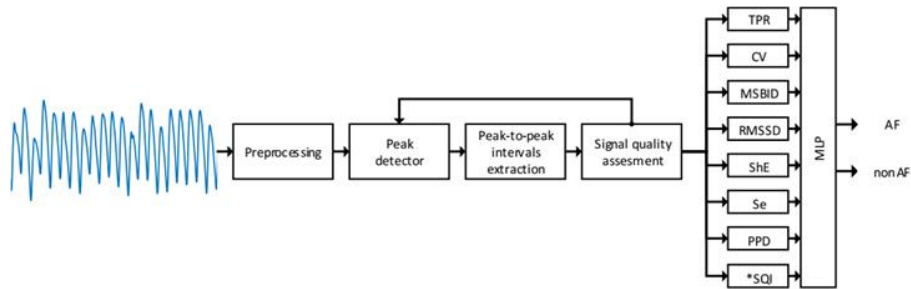


Figure 3: Structure of an MLP-based model for the AF detection task using features extracted from the PPG signal.

with AF, and bad quality without AF, respectively.

The following irregularity features are used:

- Turning point ratio (TPR)<sup>22</sup> evaluates randomness in PP intervals by identifying turning points—intervals greater or less than their two neighbours. It is computed as the ratio of turning points to total PP intervals within the analysis window. A higher TPR indicates greater randomness, aiding AF detection.
- Coefficient of variation (CV)<sup>23,24</sup> relates the standard deviation of PP intervals to their mean. In AF, increased dispersion and decreased mean duration raise CV.
- Mean successive beat interval difference (MSBID)<sup>25</sup> also links PP interval dispersion to the mean, similar to CV.
- Root mean square of successive differences (RMSSD)<sup>51</sup> measures dispersion without considering mean heart rate. It typically increases during AF.
- Shannon entropy (ShE)<sup>26</sup> quantifies signal unpredictability, rising when distribution is uniform and dropping when centered. ShE is often higher

<sup>22</sup>Dash, S., Chon, K. H., Lu, S., & Raeder, E. A. (2009). Automatic real-time detection of atrial fibrillation. *Annals of biomedical engineering*, 37, 1701-1709.

<sup>23</sup>Tateno, K., & Glass, L. (2001). Automatic detection of AF using the coefficient of variation and density histograms of RR and  $\Delta$ RR intervals. *Medical and Biological Engineering and Computing*, 39, 664-671.

<sup>24</sup>Langley, P., Dewhurst, M., Di Marco, L. Y., Adams, P., Dewhurst, F., Mwita, J. C., ... & Murray, A. (2012). Accuracy of algorithms for detection of atrial fibrillation from short duration beat interval recordings. *Medical engineering & physics*, 34(10), 1441-1447.

<sup>25</sup>Langley, P., Dewhurst, M., Di Marco, L. Y., Adams, P., Dewhurst, F., Mwita, J. C., ... & Murray, A. (2012). Accuracy of algorithms for detection of atrial fibrillation from short duration beat interval recordings. *Medical engineering & physics*, 34(10), 1441-1447.

<sup>26</sup>Shannon, C. E. (1948). A mathematical theory of communication. *The Bell system technical journal*, 27(3), 379-423.

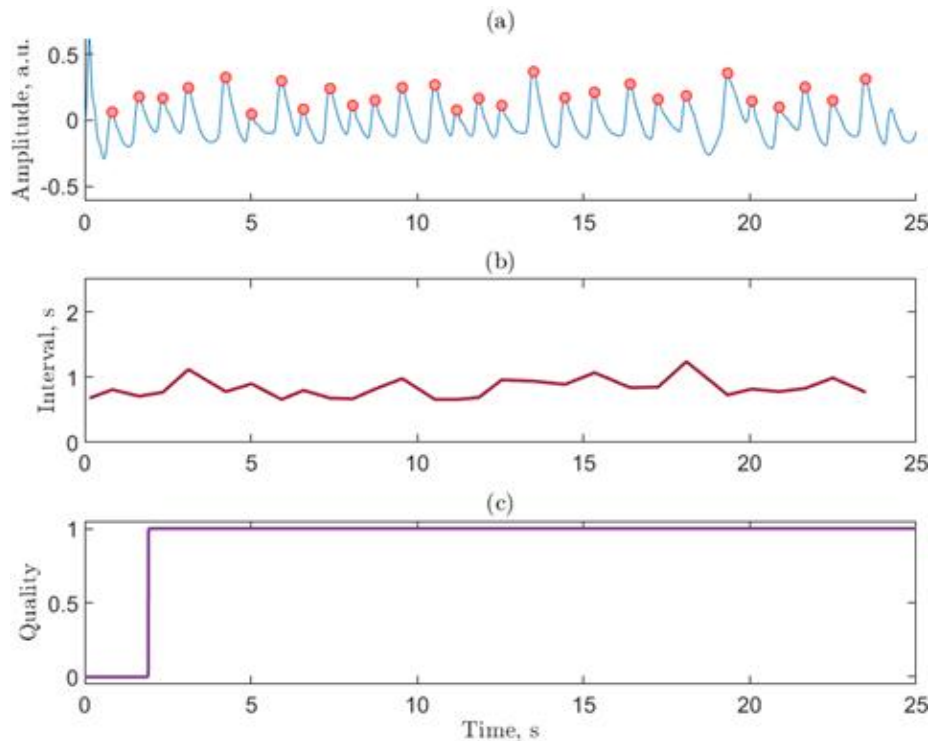


Figure 4: Good-quality PPG segment for the AF task (a) with extracted PP intervals (b) and quality index (c).

in AF than sinus rhythm.<sup>27</sup>

- Sample entropy (SE)<sup>28</sup> assesses self-similarity by calculating the probability that patterns persist in extended samples. A simplified SE is used here for efficient AF detection.<sup>29</sup>
- Poincare plot (PPD)<sup>30,31</sup> visualizes consecutive PP intervals. In AF, it shows significantly greater dispersion compared to sinus rhythm or ectopic

<sup>27</sup>Zhou, X., Ding, H., Ung, B., Pickwell-MacPherson, E., & Zhang, Y. (2014). Automatic online detection of atrial fibrillation based on symbolic dynamics and Shannon entropy. *Biomedical engineering online*, 13(1), 1-18.

<sup>28</sup>Richman, J. S., & Moorman, J. R. (2000). Physiological time-series analysis using approximate entropy and sample entropy. *American journal of physiology-heart and circulatory physiology*, 278(6), H2039-H2049.

<sup>29</sup>Petrėnas, A., Marozas, V., & Sörnmo, L. (2015). Low-complexity detection of atrial fibrillation in continuous long-term monitoring. *Computers in biology and medicine*, 65, 184-191.

<sup>30</sup>Park, J., Lee, S., & Jeon, M. (2009). Atrial fibrillation detection by heart rate variability in Poincare plot. *Biomedical engineering online*, 8(1), 1-12.

<sup>31</sup>Lian, J., Wang, L., & Muessig, D. (2011). A simple method to detect atrial fibrillation using RR intervals. *The American journal of cardiology*, 107(10), 1494-1497.

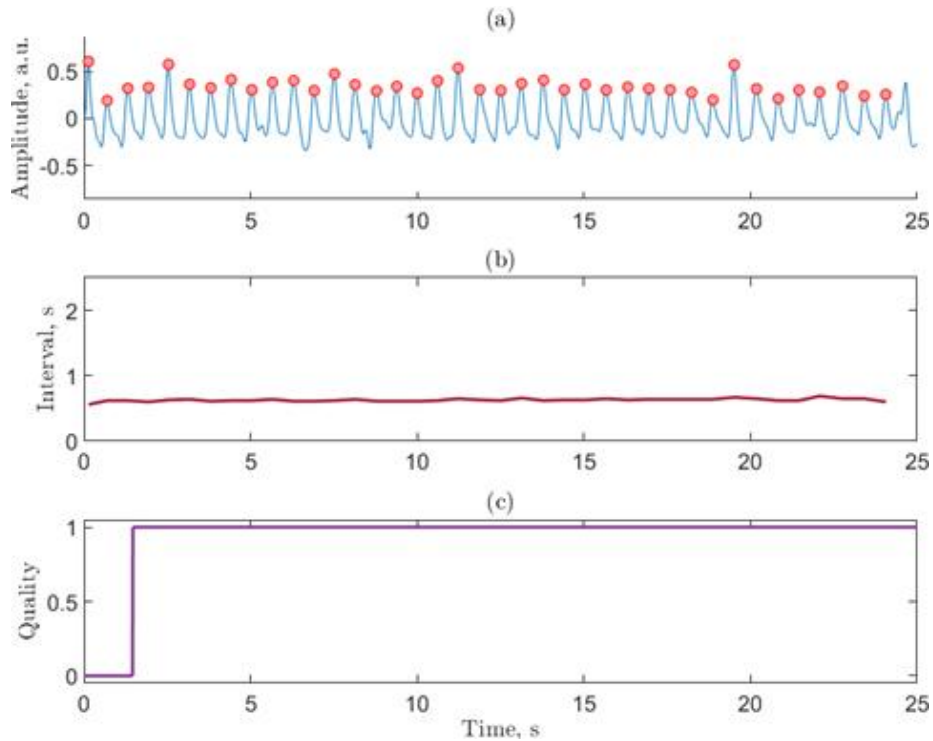


Figure 5: Good-quality PPG segment for the AF task (a) with extracted PP intervals (b) and quality index (c).

beats.

The capacity of each feature to discriminate between AF and non-AF cases is depicted in Figure 8 and Figure 9. Figure 8 shows separation of features before the removal of bad-quality PPG segments, while Figure 9 shows separation of features after the removal of bad-quality PPG segments. PPG signal quality assessment was performed using the algorithm described in<sup>32</sup>. The best visible separation of features is achieved by using SE and PPD, especially when estimated bad-quality segments are removed.

## Models

**Multilayer perceptron models** The multilayer perceptron (MLP) used for classifying features extracted from PPG signals consists of a fully connected layer with 128 neurons, followed by a ReLU activation function and a dropout layer with a 0.5 dropout rate for regularization. The network's output structure

<sup>32</sup>Sološenko, A., Petrėnas, A., Paliakaitė, B., Sörnmo, L., & Marozas, V. (2019). Detection of atrial fibrillation using a wrist-worn device. *Physiological measurement*, 40(2), 025003.

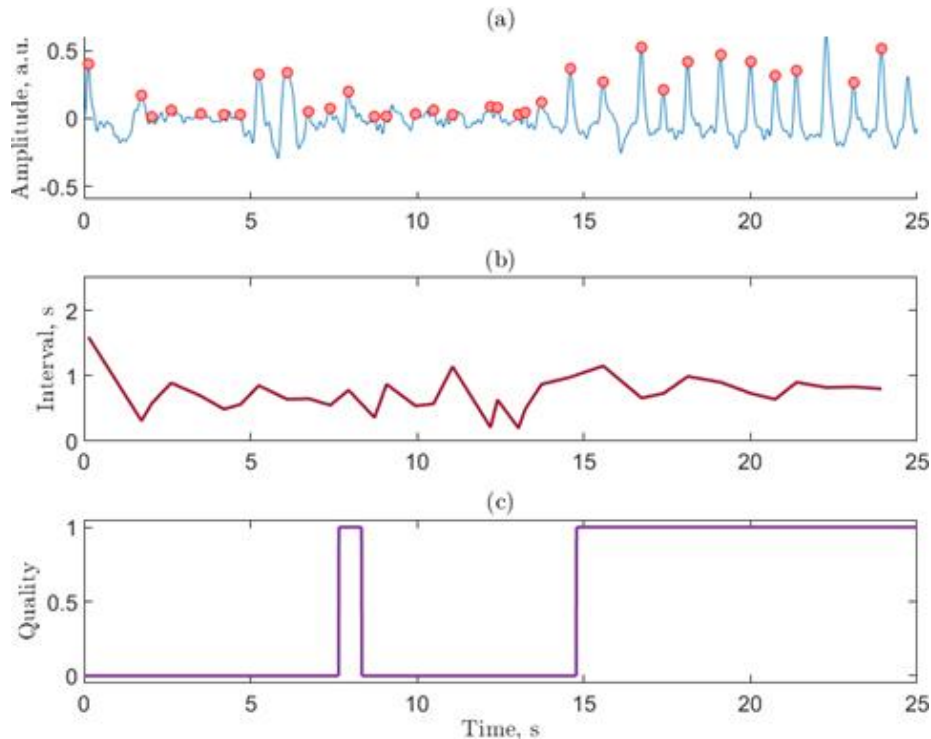


Figure 6: Bad-quality PPG segment for the AF task (a) with extracted PP intervals (b) and quality index (c).

includes a fully connected layer with 2 neurons, a softmax layer to produce a probability distribution for multi-class classification, and a classification layer for determining the final class label. The model is trained using the Adam optimization algorithm, with fixed learning rate of 0.01 and mini-batch size of 32.

**Gaussian process regression** Gaussian Process Regression (GPR) is a powerful and flexible non-parametric regression technique used in machine learning and statistics for modelling complex, nonlinear relationships<sup>33</sup>. Instead of fitting a specific function to the data, GPR models the relationship between input features and output as a distribution over functions. It incorporates prior knowledge (expressed through kernels) and provides uncertainty estimates for individual predictions. The objective of GPR is to find a mean function that accurately represents observed data points and can be used for predicting new data points. Gaussian Processes define a distribution over an infinite number of potential functions that could fit the data.

<sup>33</sup>Rasmussen, C. E. and C. K. I. Williams. Gaussian Processes for Machine Learning. MIT Press. Cambridge, Massachusetts, 2006.

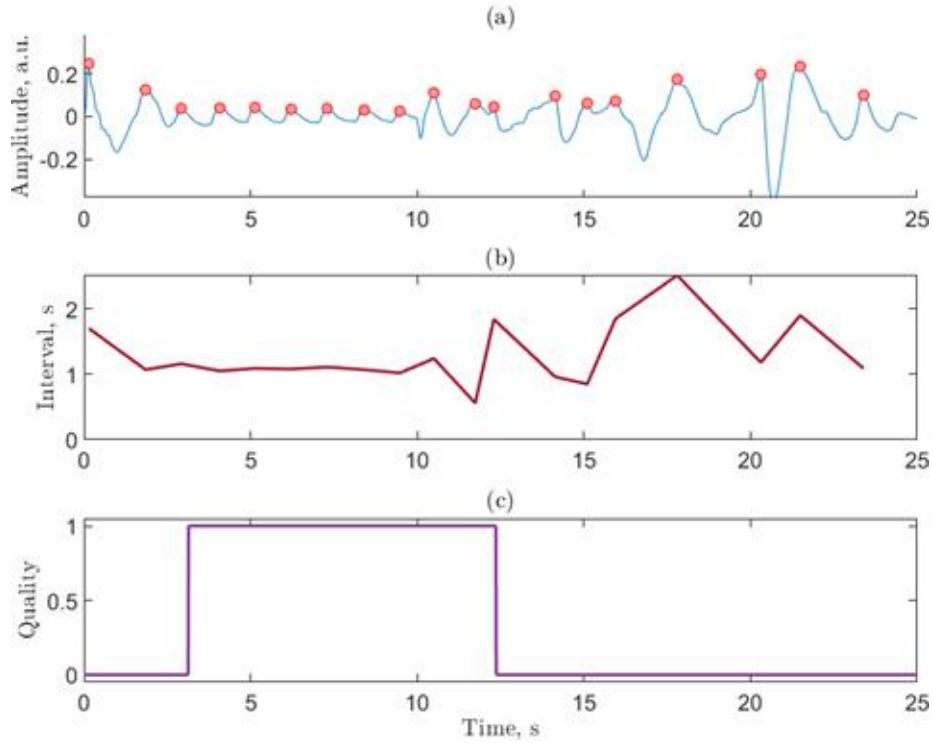


Figure 7: Bad-quality PPG segment for the AF task (a) with extracted PP intervals (b) and quality index (c).

The key points of the GPR method include the use of the Fully Independent Conditional (FIC) approximation for making predictions given the model parameters and the squared exponential kernel as the covariance function. The inter-point distance computation for evaluating built-in kernel functions was specified as the training function  $(x-y)^2$ . To ensure accurate parameter estimation, a QR-factorization-based approach was employed for computing the log-likelihood and gradient. Additionally, the limited-memory Broyden-Fletcher-Goldfarb-Shanno (LBFGS) optimizer was used for hyperparameter estimation. As a quasi-Newton method, LBFGS approximates the Hessian matrix using past gradient information, enabling rapid convergence in high-dimensional parameter spaces while maintaining computational feasibility and numerical stability. The combination of QR-factorization, the squared exponential kernel, a linear basis function, and the FIC approximation enhances the predictive performance and scalability of the model.

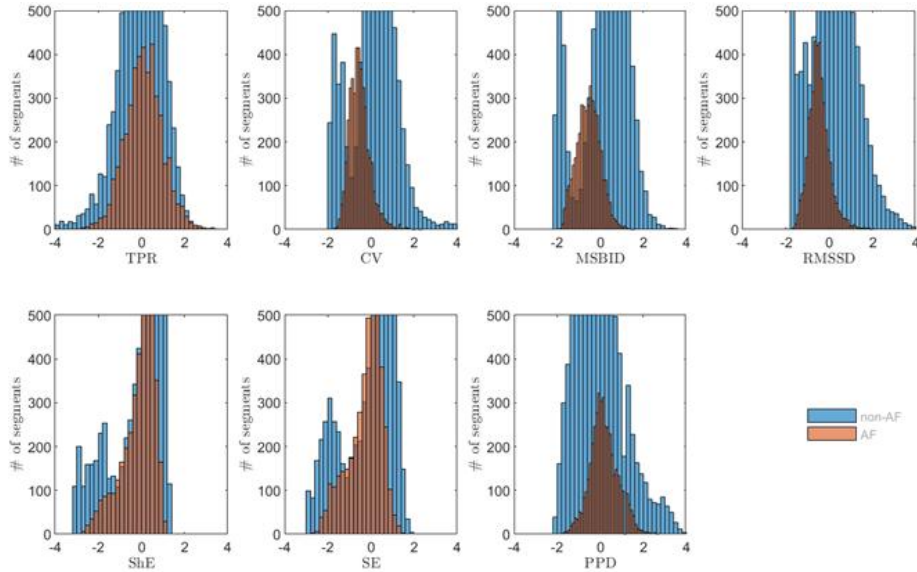


Figure 8: Discriminative capacity of each feature to distinguish between AF and non-AF cases without removing bad-quality PPG segments.

#### A.4.3 Image-Based Models

**Continuous Wavelet Transform (CWT) image representations** CWT transformation requires to define several hyperparameters among which the most important are the (1) the choice of the wavelet function, (2) the number of scales and, (3) the window size for the wavelet function at each scale. Indeed, scales affect the frequency resolution, higher scales focusing on lower frequencies and longer time windows. The number of scales defines how many different frequency bands the CWT will compute. In this project, we use a generalized morse wavelet (GMW) as the mother wavelet with a length of 1024 and 128 logarithmically spaced scales. Applying the CWT transform to PPG signals with shape  $(\langle \text{sequence\_length} \rangle, 1)$  yields a 2D array with size  $(\langle \text{sequence\_length} \rangle, 128)$  which is saved as an RGB image.

State-of-the art methods relying on CWT based scalogram as inputs, feed the CWT images to a deep learning model to perform classification/regression tasks. We propose to use the same model (ResNet18) for both BP estimation and AF detection, the only difference being the addition of a sigmoid function for AF detection.

The only input preprocessing step simply consists in resizing CWT images into squared RGB images with shape  $(224, 224, 3)$ . Such input size is typically dictated by the availability of pre-trained models commonly trained on the ImageNet dataset.

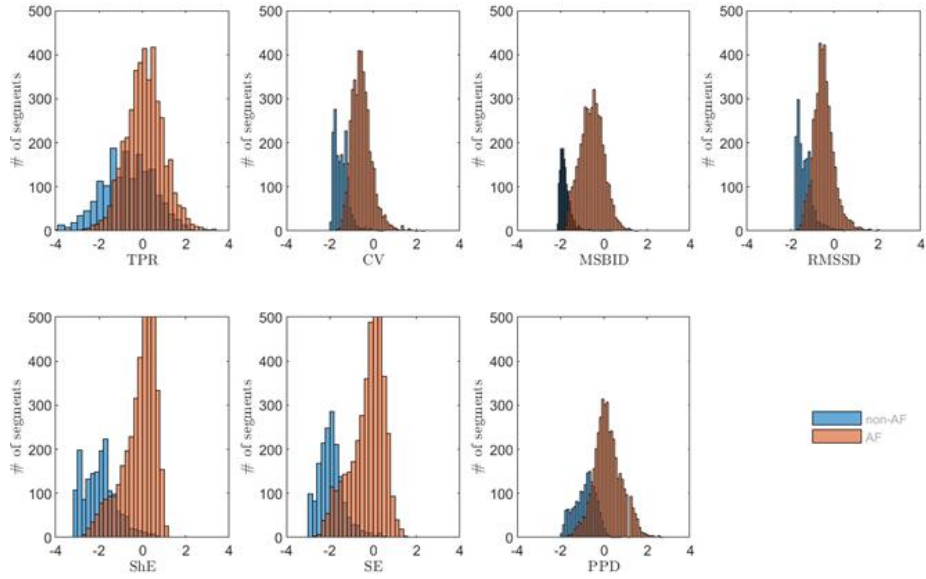


Figure 9: Discriminative capacity of each feature to distinguish between AF and non-AF cases using the removal of bad-quality PPG segments.

### STFT-Based Spectrogram Representation (Spectrogram-ResNet)

We represent PPG signals using fixed resolution time-frequency maps based on the STFT. This was done to enable modeling using convolutional neural networks. This process is placed inside the preprocessing level. Every input signal is formulated in the form of a  $(T, F)$  sequence, where  $T$  denotes the number of temporal samples and  $F$  the number of frequency bins. Moreover, to decrease the effect of boundaries on the computation of the STFT, symmetric padding is applied to both ends of the signal in the time-domain. This resulted in a channel-wise representation of power spectrograms with uniform temporal and frequency resolution. The resulting representations were organized as  $(N_{\text{windows}}, F, T)$  and subsequently converted to the logarithmic domain using decibel scaling to improve numerical stability and dynamic range. These log-power spectrograms work as input to the trained ResNet-50 or ResNet-18 CNN. The proposed Spectrogram-ResNet approach is capable of processing hierarchical information of the PPG signal in the time-frequency representation, complementing the currently existing time-domain-based models.

We represent PPG signals using fixed-resolution time-frequency maps based on the short-time Fourier transform (STFT) to enable modeling with convolutional neural networks. This processing is performed at the preprocessing stage. Each input signal is initially represented as a one-dimensional time series of length  $T$ . The STFT transforms this signal into a time-frequency representation of size  $(T, F)$ , where  $T$  denotes the number of temporal frames and  $F$  the number of frequency bins.

To reduce boundary effects during STFT computation, symmetric padding is applied to both ends of the signal in the time domain. This results in power spectrograms with uniform temporal and frequency resolution. The resulting representations are organized as  $(N_{\text{windows}}, F, T)$  and subsequently converted to the logarithmic domain using decibel scaling to improve numerical stability and dynamic range. These log-power spectrograms serve as input to the trained ResNet-50 CNN.

The proposed Spectrogram-ResNet approach captures hierarchical patterns in the PPG signal through its time–frequency representation, complementing existing time-domain-based models.

#### A.4.4 Models Parameters Count

Type	Model	AF Detection (Classification)	BP Estimation (Regression)
T	XResNet1d101	1.8 M	1.8 M
	XResNet1d50	886 K	886 K
	Inception1d	472 K	472 K
	LeNet1d	429 K	658 K
	AlexNet1d	42 M	56,7 M
	MiniRocket	30 K	30 K
	iTransformer	642 K	642 K
	TimesNet	667 K	667 K
	PPNet	125 K	125 K
	TCN+MLP	6,7 M	10,4 M
	XResNet1d50+GNLL	1,7 M	1,7 M
F	Wavelet+MLP	611 K	840 K
	CIF+MLP	1410	between 4705 to 11882
	CIF+GPR	—	32
I	CWT	11,1 M	11,1 M
	Spectrogram-ResNet	23.5 M	23,5 M

Table 10: Comparison of total parameter counts between models used for AF detection and BP estimation tasks, grouped by input representation type (**T**: time-series, **F**: feature-based, **I**: image-based, **B**: baseline).